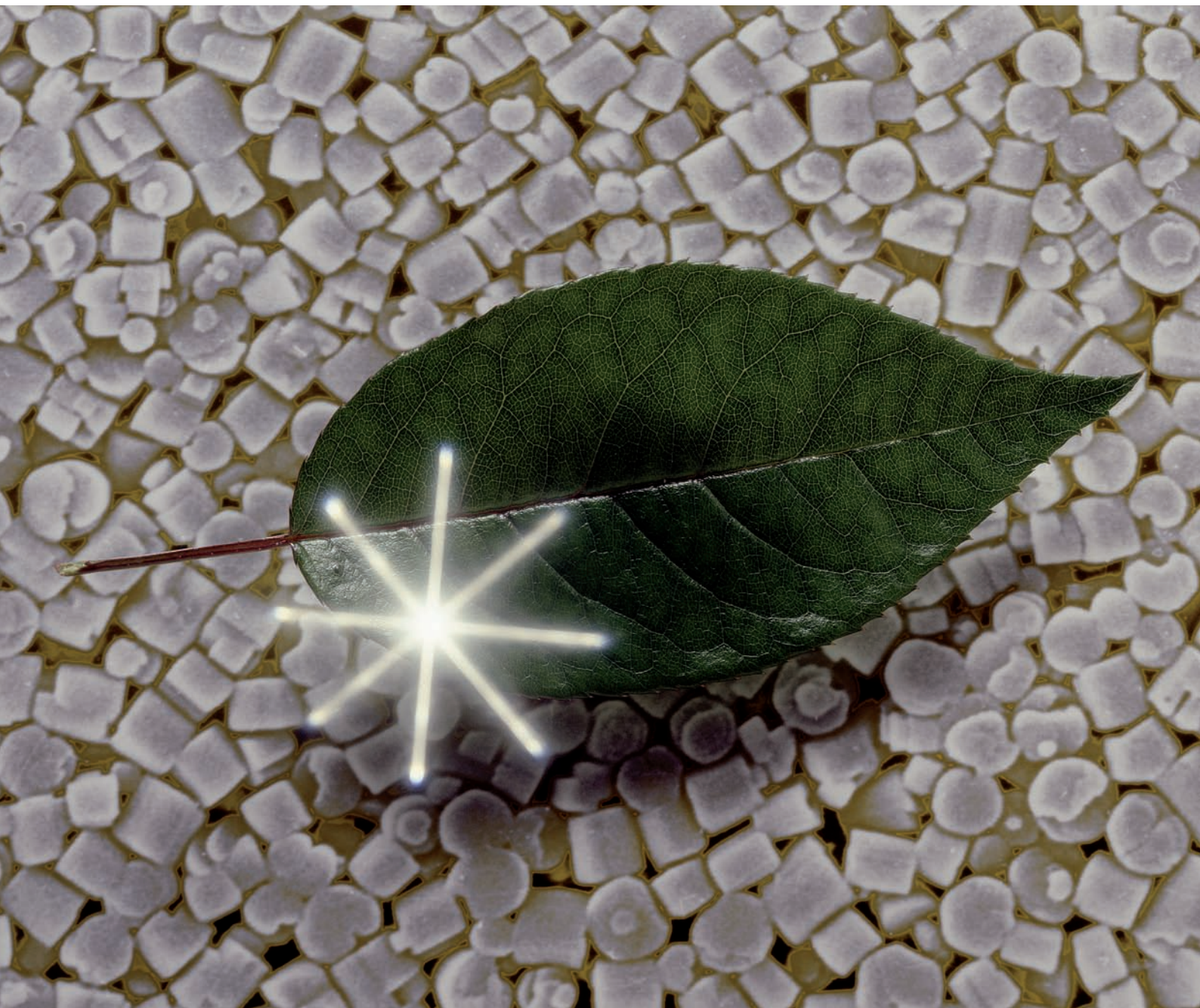


# Photochemical & Photobiological Sciences

An international journal

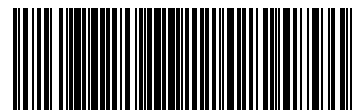
[www.rsc.org/pps](http://www.rsc.org/pps)

Volume 7 | Number 8 | August 2008 | Pages 869–992



ISSN 1474-905X

RSC Publishing



1474-905X(2008)7:8;1-Q

# Photochemical & Photobiological Sciences

The official journal of the European Photochemistry Association, the European Society for Photobiology, the Asia and Oceania Society for Photobiology and the Korean Society of Photoscience

[www.rsc.org/pps](http://www.rsc.org/pps)

RSC Publishing is a not-for-profit publisher and a division of the Royal Society of Chemistry. Any surplus made is used to support charitable activities aimed at advancing the chemical sciences. Full details are available from [www.rsc.org](http://www.rsc.org)

## IN THIS ISSUE

ISSN 1474-905X CODEN PPSHCB 7(8) 869–992 (2008)



### Cover

See Gion Calzaferri and Katsiaryna Lutkouskaya, pp. 879–910.

The cover shows a leaf on an enlarged electron microscopy image of about 700 nm large zeolite L crystals which are the host material for the artificial antenna system discussed in the article.

Image reproduced by permission of Gion Calzaferri from *Photochem. Photobiol. Sci.*, 2008, **7**, 879.

## CHEMICAL BIOLOGY

B57

Drawing together research highlights and news from all RSC publications, *Chemical Biology* provides a 'snapshot' of the latest developments in the chemical biology, showcasing newsworthy articles and significant scientific advances.

## Chemical Biology

August 2008/Volume 3/Issue 8

[www.rsc.org/chembiology](http://www.rsc.org/chembiology)

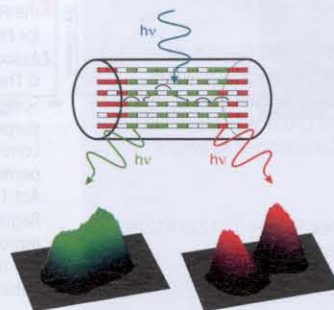
## PERSPECTIVES

879

### Mimicking the antenna system of green plants

Gion Calzaferri\* and Katsiaryna Lutkouskaya

Antenna system. The green emitting donor molecules are electronically excited. The excitation energy is transferred *via* FRET to the red emitting acceptors. The confocal fluorescence microscopy images illustrate an experimental proof of the structure shown in the scheme.



# Mimicking the antenna system of green plants†

Gion Calzaferri\* and Katsiaryna Lutkouskaya

Received 18th March 2008, Accepted 22nd May 2008

First published as an Advance Article on the web 2nd July 2008

DOI: 10.1039/b804682b

We report the preparation and investigation of hierarchically organized host–guest structures, presenting successive ordering from the molecular up to macroscopic scale, thus supporting the relationship between the molecular arrangements and the macroscopic properties. Size, shape and surface composition of the host which is zeolite L play a decisive role. Its base and coat have distinctively different chemical properties. The guests, organic dye molecules or complexes, are well oriented inside the channels and can be organized into distinctive patterns. Zeolite L crystals containing oriented fluorophores in their parallel nanochannels possess remarkable fluorescent properties and they can be arranged in nearly any desired manner by means of self-organization methods. This makes them ideal host–guest structures for the exploitation of energy transfer and energy funneling processes. Size, shape and surface composition of the objects but also the properties of the surface on which they should be organized play a decisive role. We present a simple model of an artificial antenna based on supramolecular organization of dyes in nanochannels of the host, and we explain why zeolite L can be considered as an ideal host for this purpose. The preparation of different dye–zeolite L materials is described, and Förster energy transfer experiments carried out with them. Further, increasing supramolecular organization is discussed: the first unidirectional antenna system on a macroscopic level, organization of crystals and communication of the crystals interior with the environment. Additionally, we explain spectroscopy on monolayers of dye–zeolite L micro-crystals. The materials are shown to be new building blocks for optical, electro-optical and sensing devices.

## 1. Introduction

In natural photosynthesis, sunlight is absorbed by organized chlorophyll molecules and transported to the reaction center. That is where all life begins, if we disregard some primitive organisms,

fuelled by sulfides of volcanic origin. An important aspect of natural photosynthesis is the production of oxygen. Molecular oxygen is a prerequisite of all animal and human life. Without oxygen, only primitive organisms have ever existed.<sup>1</sup> We have been working on photochemical oxidation of water to oxygen with visible light and we have devised a reversibly working photo-electrochemical water splitting process, however, its efficiency is still low.<sup>2,3</sup> The overall solar energy conversion efficiency in green plants is much lower than that of commercially available solar cells.<sup>4</sup> However, plants have many other tasks to fulfill than just

*Department of Chemistry and Biochemistry, University of Bern, Freiestrasse 3, CH-3012, Bern, Switzerland. E-mail: gion.calzaferri@iac.unibe.ch*

† Based on Theodor-Förster-Gedächtnisvorlesung presented at the International Conference on Photochemistry 2007, held 29 July–3 August 2007 in Cologne, Germany.



Gion Calzaferri

*Gion Calzaferri is emeritus professor of physical chemistry at the University of Bern (Switzerland). He is the 2007 recipient of the Theodor Förster lectureship, awarded jointly by the German Chemical Society and the German Bunsen Society for Physical Chemistry. His research focuses on supramolecularly organized molecules, clusters, and complexes in zeolites, and on artificial antenna systems for light harvesting.*



Katsiaryna Lutkouskaya

*Katsiaryna Lutkouskaya is currently a postdoctoral fellow at the Ecole Normale Supérieure de Cachan, France. She obtained her PhD from the University of Bern under the supervision of Prof. Gion Calzaferri (2007). Her research interests are photo-physical properties of molecules supramolecularly organized in zeolite L, single particle tracking, and manipulation of nanoparticles.*

storage of free enthalpy in form of chemical fuels. At the same time, the antenna system of green plants is cleverly designed and works at maximum efficiency.

The detailed structure of the antenna system of purple bacteria has been resolved. It consists of regular arrangements of chlorophyll molecules held at fixed positions by means of proteins. Light absorbed by any of these chlorophyll molecules is transported to the reaction center, providing the energy necessary for the chemical processes to be initiated.<sup>5–8</sup> A green leaf consists of millions of such well organized antenna devices. Recreating this system in the laboratory would be a hopeless task—at least regarding the current possibilities of chemists. What can be done? First we should understand the basic principles that govern transport of electronic excitation energy. Fortunately, this understanding is very advanced. It goes back to the pioneering work of Theodor Förster.<sup>9–11</sup> A chlorophyll molecule consists essentially of a positively charged backbone and some delocalized electrons. The energy of an absorbed photon is transformed into kinetic energy of one of these delocalized electrons. This fast moving electron causes an oscillating electromagnetic field. A neighboring acceptor molecule A, bearing states that are in resonance with the excited state of the donor D\*, can take over the excitation energy. Radiationless electronic excitation energy transfer taking place is due to very weak interaction between excited configurations of the initial state (D\* ··· A<sub>i</sub>) and that of the final state (D ··· A<sub>i</sub>\*).



In such a system the “optical electrons” associated with individual component molecules (or chromophoric units) preserve essentially their individual characteristic. Förster observed that the rate constant  $k_{\text{ENT}}$  for the transfer from one electronic configuration to the other can be expressed as a product of three terms: a geometrical term  $G$  that describes the distance and angular dependence of the rate constant, a term  $DA$  specific for the chromophores involved taking into account the matching of the resonance condition and the electronic transition dipole moments (ETDM) of the donor and the acceptor, and a factor  $S$  which takes the environment into account:

$$k_{\text{Ent}} \propto G \cdot DA \cdot S \quad (2)$$

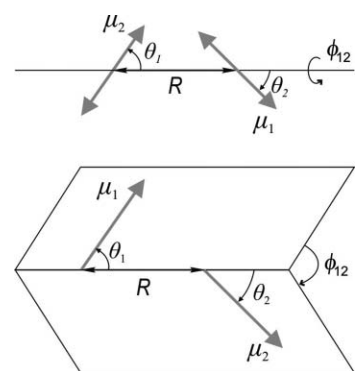
Förster explicit formula for the electronic excitation energy transfer rate constant  $k_{\text{ENT}}$  can be expressed as follows:

$$k_{\text{ENT}} = TF \frac{\kappa_{\text{D}^*\text{A}}^2 \phi_{\text{D}^*}}{R_{\text{D}^*\text{A}}^6 \tau_{\text{D}^*}} J_{\text{D}^*\text{A}} \frac{1}{n^4} \quad (3)$$

where  $R_{\text{D}^*\text{A}}$  is the distance between the donor and the acceptor,  $\tau_{\text{D}^*}$  the decay time and  $\phi_{\text{D}^*}$  the luminescence quantum yield of the donor in absence of energy transfer,  $n$  the refractive index of the environment.  $J_{\text{D}^*\text{A}}$  is the spectral overlap between the luminescence spectrum of the donor and the absorption spectrum of the acceptor, and  $\kappa_{\text{D}^*\text{A}}^2$  is the orientation factor describing the dependence of the energy transfer rate constant on the relative orientation of the ETDM of D\* and A<sub>i</sub> as illustrated in Scheme 1. The expression for  $\kappa_{\text{D}^*\text{A}}$  is

$$\kappa_{\text{D}^*\text{A}} = \sin\theta_1 \sin\theta_2 \cos\phi_{12} - 2\cos\theta_1 \cos\theta_2 \quad (4)$$

It is convenient to define the Theodor Förster constant  $TF$ , which is equal to  $8.785 \times 10^{-25}$  mol, if the spectral overlap integral  $J_{\text{D}^*\text{A}}$  is expressed in  $\text{cm}^3 \text{M}^{-1}$ , the distance  $R_{\text{D}^*\text{A}}$  in Å, the decay



**Scheme 1** Angles describing the relative orientation of the ETDM of two molecules,  $\mu_1$  and  $\mu_2$ . Top: representation of the ETDM as oscillators. Bottom: vector-representation of the ETDM. The numbers 1 and 2 also identify the two species.

time  $\tau_{\text{D}^*}$  in ns, and the rate constant  $k_{\text{ENT}}$  in  $\text{ns}^{-1}$ . Förster explicit formula for the energy transfer rate constant is the ideal limiting law for electronic excitation energy transfer. Generalization of Förster equation and extension to systems and situations where important deviations with respect to the ideal limiting law are to be expected have been made by several authors. We mention a recent paper by Scholes *et al.*,<sup>12</sup> where a better description of the solvent term than the  $n^{-4}$  approximation has been reported. For other developments we refer to ref. 5–8 but we do not intend to go further into this subject. It is important to understand that Förster theory is not exclusively valid for chlorophyll molecules but can be used to describe electronic excitation energy transfer between any molecules, clusters, quantum dots or semiconductors and combinations of them. The formula may be sufficient in its original form or can be used as first order approximation, depending on the properties of the system. We have been using the Förster equation for many years to develop ideas and to build artificial antenna systems.

We do not review the many interesting attempts of other researchers to mimic the antenna system of green plants, which are described *e.g.* in ref. 13 and 14 but describe the approach we have been following by first presenting a simple model of an artificial antenna based on supramolecular organization of dyes in nanochannels. Next we explain why zeolite L can be considered as an ideal host for supramolecular organization of dyes and how dye-zeolite L materials can be prepared. We then discuss some Förster energy transfer experiments. Increasing supramolecular organization, the first unidirectional antenna system on a macroscopic level and organization and communication are discussed next. We explain spectroscopy on monolayers of dye-zeolite L micro-crystals. The materials are new building blocks for optical, electro-optical and sensor devices.

## 2. A simple model of an artificial antenna

The design of an early model that mimics the key functionality of the antenna system of green plants was inspired by our experience with different zeolite materials. Properties of molecules, complexes and cluster inside the cavities and channels—apart from the interest in catalysis—have been investigated by several authors, see for example ref. 15–21. We reasoned that a one-dimensional channel system has the advantage of being the simplest possible

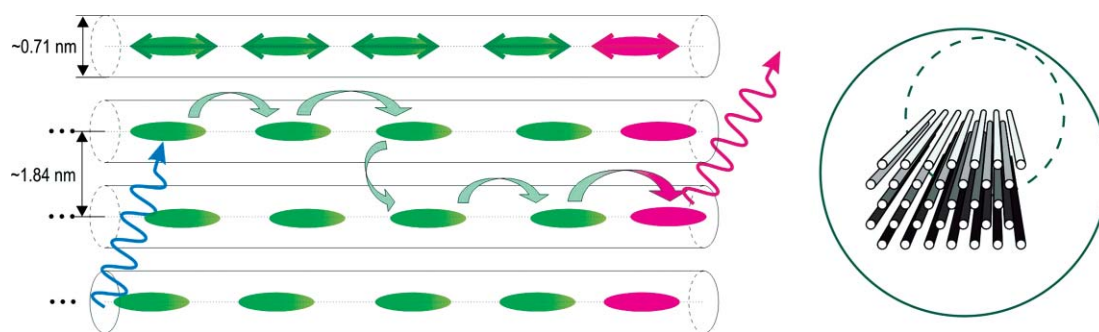


**Fig. 1** Schematic view of an artificial photonic antenna. The chromophores are embedded in the channels of the host. The green dyes act as donor molecules which absorb the incoming light and transport the excitation *via* Förster energy transfer to the red acceptors shown at the ends of the channels on the right. The process can be analyzed by measuring the emission of the red acceptors and comparing it with that of the donors. Right: top view of a bunch of such strictly parallel channels.<sup>25,26</sup>

choice. As a consequence, we considered zeolite L which was well known. It started with investigations on the insertion and structure of cationic dyes into the channels of zeolite L.<sup>22–24</sup> In a theoretical and preliminary experimental study, we examined cylinders containing green emitting donor molecules and at ends red emitting acceptors.<sup>25,26</sup> Later we carried out many experiments based on this.<sup>27,28</sup> Our basic reasoning can be illustrated by means of Fig. 1. The donor molecules are represented in green and the acceptors in red. The donor that has been excited by absorbing an incident photon transfers its electronic excitation to an unexcited neighbor. After series of such steps, the electronic excitation reaches a luminescent trap (acceptor molecule) and is then released as fluorescence. The acceptors are thought to mimic the “entrance of the reaction center RC” of the natural antenna. The dimensions given in Fig. 1 correspond to the pore opening and the distance between the centers of two channels in zeolite L. According to Förster theory, the largest energy transfer rate constant is observed if the ETDM are oriented parallel to the channel axis. For this situation the factor  $\kappa^2_{D^*A}$  has its maximum value of 4. Realization of this system in the laboratory seemed to be feasible. One of the questions was, whether one dimensional (1D) energy transfer would occur, because this would lead to a very efficient light harvesting material.<sup>25,26</sup>

### 3. Dye–zeolite L materials

#### 3.1. Zeolite L

Zeolite L has been found to be an ideal host for supramolecular organization of dyes. Its structure and morphology is explained in Fig. 2 and 3.<sup>29–35</sup> The primary building units of classical zeolites are  $\text{TO}_4$  tetrahedra where T is equal to Al or Si, Fig. 2(A). Connecting them by means of oxygen bridges one obtains a secondary building unit, in the present case the cancrinite cage shown in Fig. 2(B)–(D). Cancrinite cages are stacked into columns along the *c*-axis as shown in Fig. 2(E), and these columns are connected in the *a,b*-plane, Fig. 2(F) and Fig. 2(G), resulting in a the system of 1D parallel channels characteristic for zeolite L. The arrangement of the channels is hexagonal as is also nicely seen in the TEM-diffraction pattern of the standing crystal in Fig. 3(B). The stoichiometry of zeolite L is  $(\text{M}^+)_9[(\text{AlO}_2)_9(\text{SiO}_2)_{27}] \cdot n\text{H}_2\text{O}$ , where  $\text{M}^+$  are monovalent cations (blue and green balls in Fig. 2(G)) compensating the negative charge resulting from the

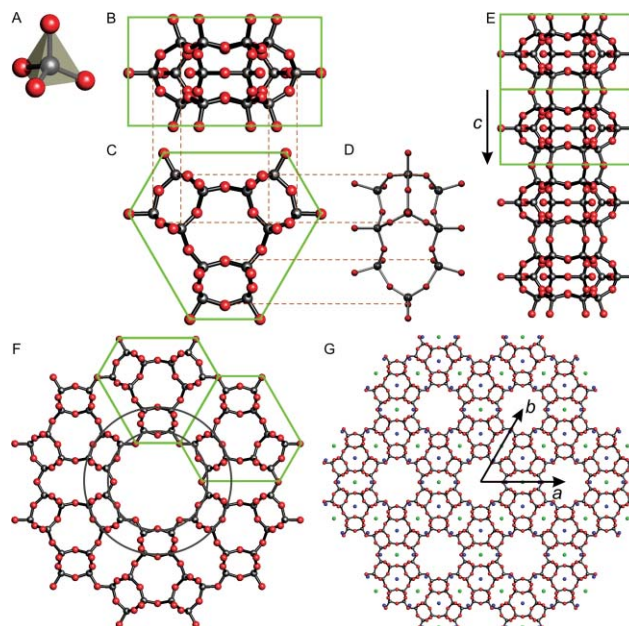


**Fig. 2** Structure of zeolite L. (A) Primary building unit,  $\text{TO}_4$  tetrahedron. Grey spheres are Si or Al atoms, red are oxygen atoms. (B)–(D) Secondary building unit, cancrinite cage (18 corner-sharing  $\text{TO}_4$  tetrahedra). (E) Stacking the cages along the *c*-axis of the crystal. The length of the vector *c* is 7.5 Å. (F) Top view of a 1D channel; cancrinite cages are connected in a plane perpendicular to the *c*-axis (*a,b*-plane). The two grey circles mark the shortest and the largest channel openings, 7.1 and 12.6 Å, respectively. (G) Channel system. Blue and green balls represent charge compensating cations. The length of the vectors *a* and *b* is 18.4 Å. This is also the center to center distance between two channels.

aluminium atoms. *n* is 21 in fully hydrated materials, and 16 at about 22% relative humidity.

We have learned how to synthesize zeolite L crystals in the size range of 30 nm up to about 10 000 nm, which means that we can cover about 7 orders of magnitude in terms of volume.<sup>36–38</sup> Electron microscopy images in Fig. 3(A) give an impression of the variety of size and morphology of zeolite L materials available: (1) is a transmission electron microscopy (TEM) image of *nanocrystals* in the size range 30–60 nm, recently also known as *Lucidot*.<sup>39</sup> It is followed by scanning electron microscopy (SEM) images of *nanodiscs* (2) with an average length of 65 nm and an average

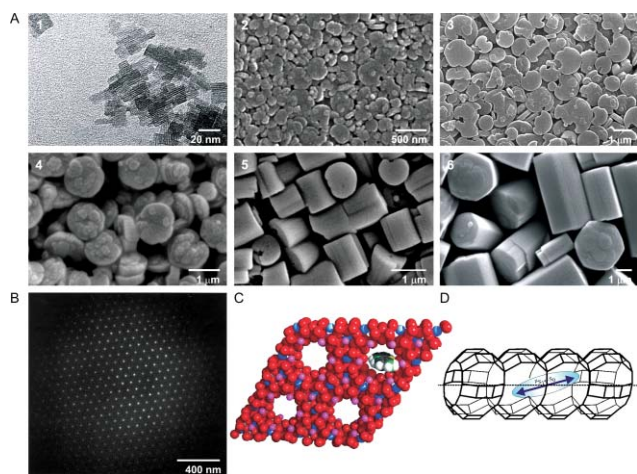


**Fig. 3** Morphology and structural features of zeolite L. (A) Electron microscopy images of zeolite L materials: (1) TEM image of nanocrystals; (2)–(6) SEM images: (2) nanodiscs, (3) and (4) two different types of disc-shaped zeolite L, (5) can-shaped crystals (about equal length and diameter) and (6) large crystals. (B) TEM-Diffraction pattern of the standing crystal demonstrating the hexagonal arrangement of the channels. (C) van der Waals picture of a dye molecule entering a channel. (D) Side view of a channel with a molecule inside. The double arrow indicates the ETDM of the molecule.

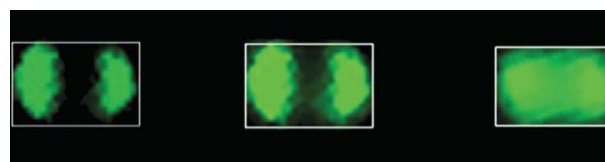
diameter in the order of 300 nm; (3) and (4) show two different types of *disc-shaped zeolite L crystals* with an average length of 200 and 350 nm, respectively, and an average diameter of about 1 μm; (5) are *can-shaped crystals* of about equal length and diameter around 1 μm, and (6) is an example of somewhat *larger crystals* of 5 μm average length and of 2 to 3 μm diameter. It is useful to imagine zeolite L as consisting of a bunch of strictly parallel channels as shown in Fig. 1(right). The channels have a smallest free diameter of about 7.1 Å, the largest diameter inside is 12.6 Å. The distance between the centers of two channels is 18.4 Å. Each zeolite L crystal consists of a large number of channels  $n_{\text{ch}}$  which can be calculated as follows:

$$n_{\text{ch}} = 0.267(d_z)^2 \quad (5)$$

where  $d_z$  is the diameter of the crystal in nm.<sup>27</sup> For example, a crystal of 600 nm diameter consists of nearly 100 000 strictly parallel channels. The ratio of the void space available in the channels with respect to the total volume of a crystal is about 0.26. The van der Waals picture in Fig. 3(C) illustrates a dye molecule of the size of thionine ( $\text{Th}^+$ ) entering a channel of zeolite L. We see that  $\text{Th}^+$  molecules can enter the channel, once they are inside, however, the space is too tight for them to pass each other. An important consequence is that zeolite L allows realizing extremely high concentrations of well oriented molecules that behave essentially as monomers. A 30 nm crystal can bear nearly 5 000 dye molecules that occupy 2 u.c., while a 60 nm crystal can host nearly 40 000. This is extremely interesting! Fig. 3(D) shows a side view of a channel with a molecule inside. The double arrow indicates a possible orientation of the molecules ETDM which can be parallel to the channel axis, perpendicular to it, or at any angle in-between, depending on the length and the shape of the molecule.

### 3.2. Insertion of dyes into the channels of zeolite L

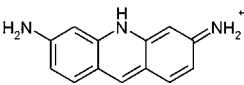
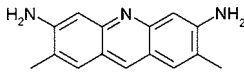
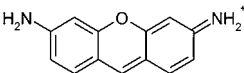
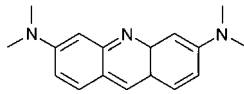
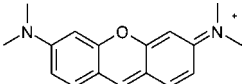
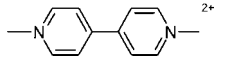
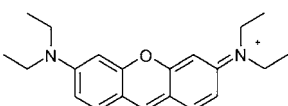
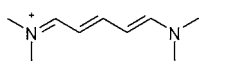
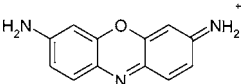
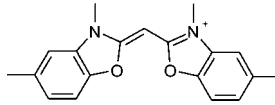
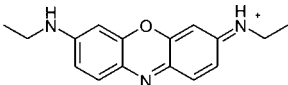
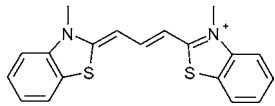
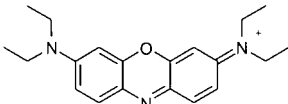
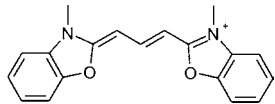
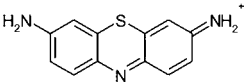
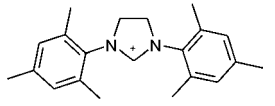
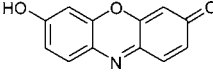
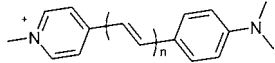
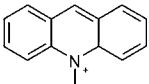
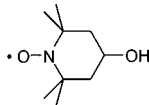
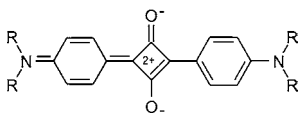
Insertion of dyes into the channels of zeolite L can be realized in different ways: by cation exchange for cationic dyes, or from the gas phase for neutral dyes. In some cases also insertion from an appropriate solvent can be used. Cation exchange can be carried out from different solvents. Choice of the right solvent and temperature may be critical. A typical procedure for the insertion of neutral molecules is to dry the zeolite under vacuum and then to sublime the dye, again under vacuum. The temperature can range from about 80 °C up to 350 °C, depending on the dyes, the size of the zeolite crystals and the material envisaged. A crucial step in the preparation of good dye zeolite materials consists in eliminating dyes that are adsorbed at the outer surface. The general procedure is to remove them by means of an appropriate solvent, without, however, washing out the dyes that are inside the channels. For details we refer to ref. 27, 40–46. Examples of cationic and neutral dye molecules that fit well into the channels are reported in Tables 1 and 2. It is usually not possible to insert negatively charged dyes into the negatively charged channels of zeolite L. The only example known to us is resorufin which has been inserted in its neutral form ResH and then deprotonated. It was observed to have interesting properties.<sup>21,46</sup> Control of the transport kinetics of dyes inside the channels is necessary if a homogeneous distribution is desired, since diffusion can be hindered due to space restriction and therefore be slow at room temperature. A way to monitor the kinetics is by observing the process in a fluorescence microscope.<sup>47</sup> We illustrate this in Fig. 4 where we show images of a 1300 nm crystal loaded with some  $\text{Py}^+$  molecules after different reaction times. We observe that all dyes are located at both ends at the beginning and that they travel deeper and deeper into the channels upon heating. Heating of a 1-butanol dispersion is less effective than heating in the oven. This illustrates that not only the temperature but also the environment influences the transport kinetics. It is usually easier and faster to realize homogeneous loading of long crystals in the gas phase (loading of neutral dyes), because the insertion can be realized at higher temperature and the channels do not contain solvent molecules.



**Fig. 4** Transport kinetics of  $\text{Py}^+$  in a 1300 nm crystal. Left: after 24 h exchange at 60 °C. Middle: after treating the same crystal for 2 h in 1-butanol at 85 °C. Right: after putting the crystal for additional 2 h in the oven at 85 °C. The loading was about 0.01, see eqn (6) and (7).

It is difficult to obtain good X-ray based information of dyes inside of the channels because the crystals of interest are usually small and translational symmetry is often not present or even not desired. There are some exceptions reported in ref. 48–51. IR, Raman and luminescence spectroscopy on powders, layers or monolayers, or on single crystals by using different optical microscopy techniques and recently also transmission spectroscopy on oriented monolayers are the most powerful tools available for obtaining detailed information on the location, orientation and

**Table 1** Cationic and some special dyes

Name/abbreviation	Structural formula	Name/abbreviation	Structural formula
Proflavine <sup>+</sup>		AY	
Py <sup>+</sup>		AQ	
PyGY <sup>+</sup>		MV <sup>2+</sup>	
PyB <sup>+</sup>		BDP <sup>+</sup>	
Ox <sup>+</sup>		MC <sup>+</sup>	
DEOx <sup>+</sup>		PC20 <sup>+</sup>	
Ox1 <sup>+</sup>		PC21 <sup>+</sup>	
Th <sup>+</sup>		BTMPI <sup>+</sup>	
ResH		DSM <sup>+</sup> (n = 1)	
MeAcr <sup>+</sup>		Hydroxy-TEMPO	
		SQ III, R = CH <sub>3</sub> SQ(JG9), R = (CH <sub>2</sub> ) <sub>3</sub> CH <sub>3</sub>	

other properties of the molecules in the channels. Some of this will be discussed in the next sections. The photophysical and photochemical behavior of a molecule depend on the loading, the co-cations and the solvent present. The influence of the proton activity inside the channels of zeolite L has been discussed recently in detail.<sup>45</sup> The influence of the co-cations is especially important in absence of solvent molecules inside the channels. Under such conditions pronounce heavy atom effect can lead to very high phosphorescence yield.<sup>52-55</sup> Here, we focus on fully hydrated dye-

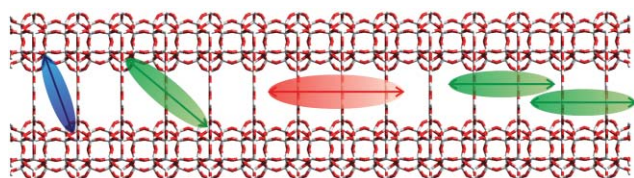
zeolites L materials. This means that each unit cell contains water molecules.

### 3.3. Orientation of dyes inside the channels

The geometrical constraints imposed by the host determine the orientation of the dye molecules. This results in a preferred orientation of the ETDM inside the channel. Some situations are illustrated in Scheme 2 where we show a simplified view of

**Table 2** Neutral dyes

Name/abbreviation	structural formula	Name/abbreviation	Structural formula
BP		Naphtalene	
<i>p</i> TP		Anthracene	
DPH		ResH	
PBOX		<i>N</i> -Ethylcarbazole	
MBOXE		Fluorenone	
POPOP		DCS	
DMPOPOP		Stilbene	
Isoviolanthron		Azobenzene	
Solvent Green 5		DANS	
PR 149		NY43	
DXP		JCG65	
Perylene-73		Hostasol Red	
		Hostasol Yellow	



**Scheme 2** Orientations of molecules inside a channel and their ETDM (double-arrow). The molecule on the left is small enough to fit into one unit cell and its shape is such that the ETDM is oriented nearly perpendicular to the channel axis. Then we see a molecule that occupies two unit cells and is oriented at about  $45^\circ$ . The next is so large that it can only align parallel to the  $c$ -axis of the crystal. On the right we illustrate a situation where two molecules come so close that their orientation and their optical properties are influenced by the packing.

a zeolite L channel containing different dyes. The orientation of their ETDM is indicated by a double arrow.

The double cone shown in Fig. 5(A) is often a good way to describe the orientation of an ensemble of dyes inside the channels. The double-arrows represent possible orientations of the ETDM, as in Scheme 2, and  $\beta$  describes the half opening angle of the double cone, *i.e.* the angle it forms with respect to the channel axis. The orientation of the ETDM, which is typically parallel to the molecules' long axis, can be examined by means of fluorescence microscopy.<sup>56</sup> By inserting a polariser in front of the detector, polarized images are obtained. In Fig. 5(C), the theoretical relative intensity of the observed fluorescence is plotted *versus* the angle  $\varepsilon$  between the observed polarisation and the crystal  $c$ -axis for different values of  $\beta$ . The fluorescence images in Fig. 5(D)–(F) show crystals of about  $2\ \mu\text{m}$  length oriented perpendicularly to each other. Images in the left column are observed without using a polarizer, while in the middle and right column the fluorescence was observed through a polarizer, the direction of which is indicated by the white double-arrow.  $\beta = 90^\circ$  indicates that the ETDM is perpendicular to the crystal axis. The double-cone distribution of the ETDM orientations reduces to a plane as shown in Fig. 5(D). According to the theoretical intensity distribution, Fig. 5(C), fluorescence reaches the maximum when the polarizer is set at the angle  $\varepsilon = 90^\circ$  with respect to the crystal axis. MeAc<sup>+</sup>–zeolite L is an example of a perpendicular arrangement.<sup>44</sup> The crystal appears bright when observed perpendicular to the crystal axis and remains dark, if the polariser is set parallel to it. If  $\beta = 0^\circ$ , the double cone distribution reduces to a line, Fig. 5(F). The maximum fluorescence intensity is observed parallel to the  $c$ -axis, and the crystal emits no light perpendicular to it. The DCS–zeolite L and POPOP–zeolite L show this behaviour. For  $\beta$  between  $0^\circ$  and  $90^\circ$ , the behaviour of fluorescence intensity changes from one extreme case to the other, and the differences between the maximum and minimum fluorescence intensity flattens. At the magic angle of  $54.7^\circ$  no fluorescence anisotropy can be observed although the orientation of the electronic transition moments is ordered and not randomly distributed in the crystal. Three examples are shown in Fig. 5(E). The orientation of the Py<sup>+</sup> ETDM in zeolite L is  $72^\circ$ .<sup>56</sup> In the case of longer molecule, PyGY<sup>+</sup>, we hardly observe any angle dependence.<sup>27</sup> This means that the orientation of the ETDM is close to the magic angle. In the case of PyB<sup>+</sup>–zeolite L, the intensity has its maximum parallel to the  $c$ -axis, and the difference between maximum and minimum is large.

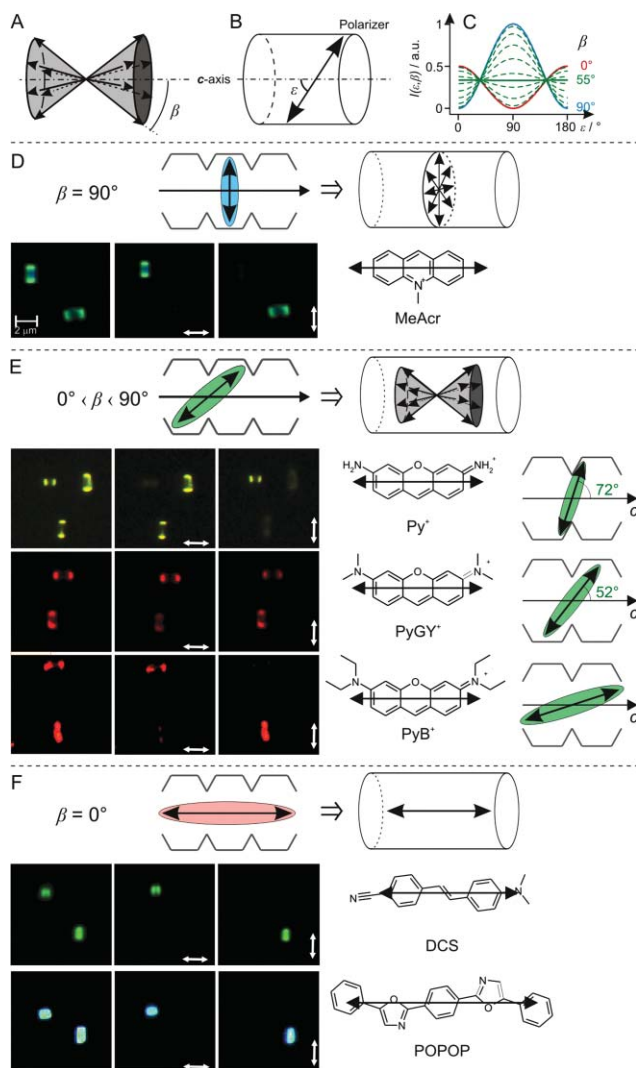
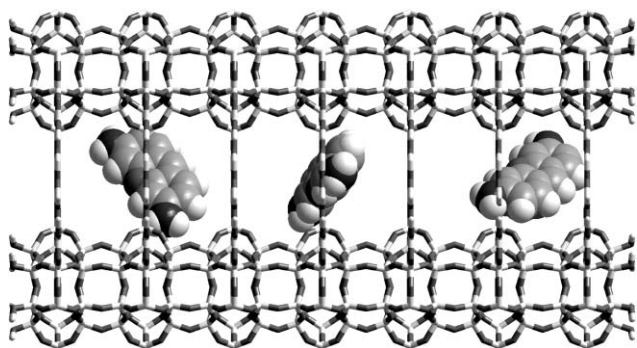


**Fig. 5** Orientation of ETDM of dye molecules inside the channel. (A) Distribution of the ETDM on a double cone with a half opening angle  $\beta$ . (B) Polarisation direction observed when the fluorescence of a single crystal is examined by means of a polariser. (C) Relative intensity of the observed fluorescence as a function of the observation angle  $\varepsilon$  with respect to the  $c$ -axis, for different half cone angles  $\beta$ . (D)–(F): Different orientations of the ETDM of dye molecules and view of the double cone distribution: (D) Perpendicular to the channel axis,  $\beta = 90^\circ$ . The double cone distribution of the dye molecules reduces to a plane. (E)  $0^\circ < \beta < 90^\circ$ . (F) Along the channel axis,  $\beta = 0^\circ$ . The double cone distribution reduces to a line.

The double cone distribution is easy to understand for medium and small angles. It is more difficult to visualize and understand it for larger angles such as observed for Py<sup>+</sup> or Ox<sup>+</sup>. We illustrate this in Scheme 3 which shows three Py<sup>+</sup> molecules oriented at about  $72^\circ$  in a channel, in a cone shaped distribution manner. The double cone distribution may not always be valid for small dye molecules that fit into a single unit cell.

From the whole volume of the zeolite only a part, namely the channels, is available for the guest species. Therefore, it is convenient to introduce a parameter bearing the information on dye concentration but based on purely geometrical (space-filling) properties of the zeolite as a host, *i.e.* showing to which extent the zeolite channels are filled with dye molecules. The *loading*, or



**Scheme 3** Three  $\text{Py}^+$  molecules with their electrical dipole arranged at about  $73^\circ$  with respect to the  $c$ -axis.

occupation probability,  $p$  of a dye–zeolite L material is defined as follows

$$p = \frac{\text{number of occupied sites}}{\text{total amount of sites}} \quad (6)$$

where the *site*  $n_s$  is the number of unit cells occupied by the dye molecule; it can be 1, 2, 3 *etc.* The loading ranges from 0 for an empty zeolite to 1 for a fully loaded one. The dye concentration of a dye–zeolite material  $c(p)$  can be expressed as a function of the loading as follows:

$$c(p) = 0.752 \frac{p}{n_s} \left( \frac{\text{mol}}{\text{L}} \right) \quad (7)$$

### 3.4. Packing of the dyes inside the channels

The packing of the dyes inside the channels influences the material properties considerably. Dimers can be formed if the molecules are sufficiently small like *e.g.* naphthalene.<sup>20</sup> We focus on molecules that are too large for this. They may, however, still be of a size, that allows them to come close enough so that *e.g.* coupling of the electronic transition moments<sup>57–61</sup> can be significant, as has recently been reported by Busby *et al.* in time-space and spectrally resolved microscopy experiments on single micrometer sized crystals.<sup>62</sup> This can be prevented, if desired, by using *e.g.* dye molecules with sufficiently bulky substituents at both ends so that the intermolecular distances remain too large even at high packing for such coupling to be important. Some situations are illustrated in Scheme 2.

We show in Fig. 6 excitation and luminescence spectra of  $\text{PC21}^+$ –zeolite L samples of different loading and compare them with the absorption spectrum of a  $10^{-6}$  M solution and the luminescence spectrum of a  $\text{PC21}^+$ –zeolite L sample with 0.045 loading (green lines). With increasing loading the excitation band, Fig. 6(left), splits into a shorter and a longer wavelength components, at 452 nm and 493 nm, respectively. Two additional bands appear in the emission spectrum, one at 540 nm and a second at 572 nm, Fig. 6(right). At high loading the additional band at 572 nm becomes the most prominent one and shifts slightly to the red, from 572 to 578 nm.  $\text{PC21}^+$  has a very high extinction coefficient of  $165\,900 \text{ M}^{-1} \text{ cm}^{-1}$ , and its oscillator strength is equal to 1.4, hence, the  $J$ -aggregate coupling can be considerable.

$\text{PC21}^+$  enters the channels reluctantly. The actual procedure we have been using to insert it was to reflux a  $n$ -octane suspension containing zeolite crystals and an excess of the dye at  $110^\circ\text{C}$  for 18 h. Based on this, on the spectroscopic observations in Fig. 6, and

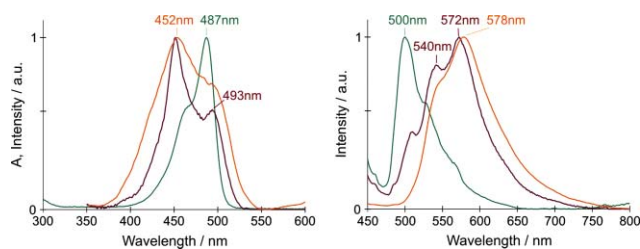
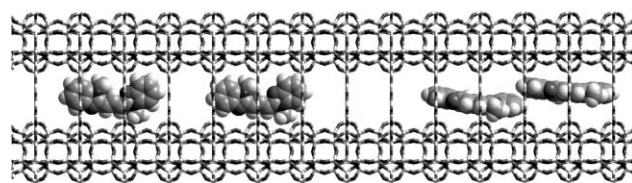


**Fig. 6** Absorption, excitation and emission spectra of  $\text{PC21}^+$  scaled to 1 at the peak maxima. Left: Absorption spectrum of  $\text{PC21}^+$  in  $10^{-6}$  M solution (green line), excitation spectra of  $\text{PC21}^+$ –zeolite L at  $p = 0.068$  (deep red line, emission observed at 540 nm) and  $p = 0.18$  (orange line, emission observed at 640 nm). Right: Emission spectra of  $\text{PC21}^+$ –zeolite L at  $p = 0.045$  (green line), at  $p = 0.068$  (deep red line) and  $p = 0.18$  (orange line).<sup>63</sup>

on the observation in a fluorescence microscope that the emission of the  $\text{PC21}^+$ –zeolite L crystals is polarized parallel to the  $c$ -axis, we can deduce the situation depicted in Scheme 4, where we show on the left the non interaction situation and on the right the stacking of the molecules which occurs at higher packing. The situation is similar but more pronounced as reported in ref. 62.



**Scheme 4** Illustration of  $\text{PC1}^+$  molecules in a channel of zeolite L. Left: non-interacting molecules. Right: stacking occurring at higher loading.

The  $J$ -aggregate coupling strength  $\beta_c$  and therefore the splitting of the levels depend on the relative orientation of the ETDM  $\mu_{AA^*}$ , expressed as  $\kappa_{A^*A}$  eqn (4), Scheme 1, the distance  $R$  and the refractive index  $n$  of the medium.<sup>61</sup>

$$\beta_c = \frac{1}{4\pi\epsilon_0 n^2} \frac{|\mu_{AA^*}|^2}{R^3} \kappa_{A^*A} \quad (8)$$

The coupling is largest for in-line orientation and changes sign for parallel orientation at a given distance. We illustrate this by means of the correlation diagram in Fig. 7, which shows the exciton splitting in a molecular dimer caused by the interaction of the configurations *via* the ETDM. In-line arrangement of the ETDM leads to J-coupling while H-coupling occurs at essentially parallel arrangement.

The electronic transition  $\Phi_+ \leftarrow \Phi_0$  to the lower lying state is allowed in the inline J-coupling while that to the higher lying  $\Phi_-$  state is forbidden. The energy of the states is reversed in case of H-arrangement. The situation is more complex if the geometry deviates from these limiting cases. We therefore show in Fig. 8 the angle dependence of the magnitude of the oscillator strength for the + and for the – phase situation. The angles  $\theta_1$  and  $\theta_2$ , shown in Scheme 1, have been chosen to be equal for both interacting ETDM, which is probably often relevant inside of the channels due to space restrictions. It explains the splitting of the absorption band of  $\text{PC21}^+$  show in Fig. 6 (left).

Eqn (8), Fig. 7 and 8 refer to a pair  $(A^* \cdots A) \leftrightarrow (A \cdots A^*)$ . More extended interaction schemes are expected to be possible

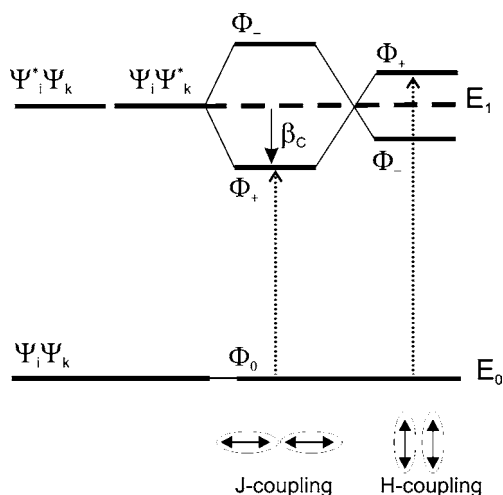


**Fig. 7** Correlation diagram, illustrating the exciton splitting, caused by the interaction of the ETDM of two molecules. This interaction naturally causes only a splitting of electronically excited states and has no consequences on the ground state. The different splitting of the excited state levels for ETDM oriented in-line (J-coupling) or parallel (H-coupling), as represented by means of double arrows, is due to the angle dependence of  $\kappa_{AA^*}$ . The allowed electronic transitions are indicated by the dotted arrows.

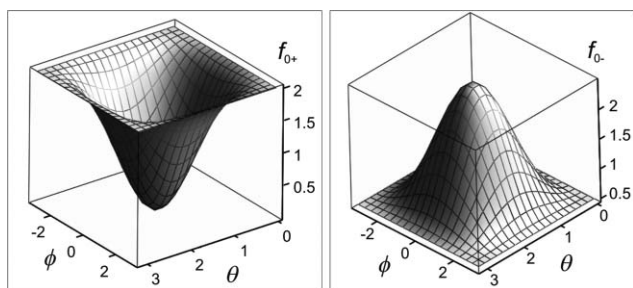
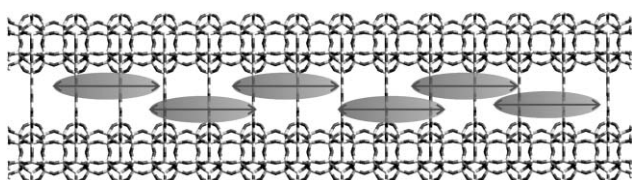


**Fig. 8** Angle dependence of the magnitude of the oscillator strength  $f_{0+}$  and  $f_{0-}$ , scaled with respect to  $f = 1$  for the free molecules.

inside the channels of zeolite L, as illustrated in Scheme 5. In this case energy bands develop. Only preliminary observations indicating such situations are currently available. There is little doubt that such real one-dimension exciton band-systems inside of the channels of zeolite L will be found.



**Scheme 5** Stacking of molecules of appropriate size and shape inside a channel and their ETDM (double-headed arrow), leading to extended exciton states of large coherence length.

### 3.5. Self-absorption

Considerable self-absorption causing large changes in the fluorescence spectrum may occur because zeolite crystals can be packed densely with dye molecules which leads to high absorption depth of individual crystals. Self-absorption means that a certain amount

of the emitted radiation is re-absorbed by the compound. This happens to photons emitted within the spectral overlap region. These photons have the right energy to be re-absorbed which means that a photon that has been emitted by one dye molecule can be absorbed by another one.<sup>64</sup> Self-absorption leads to a change in the spectral distribution: the fluorescence intensity in the spectral overlap region is lower with respect to the intensity of the rest of the spectrum. This is seen in Fig. 9(top) where the fluorescence spectra of two DXP solutions,  $4 \times 10^{-7} \text{ mol L}^{-1}$  (solid) and  $5 \times 10^{-6} \text{ mol L}^{-1}$  (dotted), measured in a 1 cm cuvette at rectangular excitation-observation geometry are presented. The spectra are scaled in the region where self-absorption does not take place. We clearly see that the intensity of the short-wavelength region of the more concentrated solution is considerably lower than that of the less concentrated one.

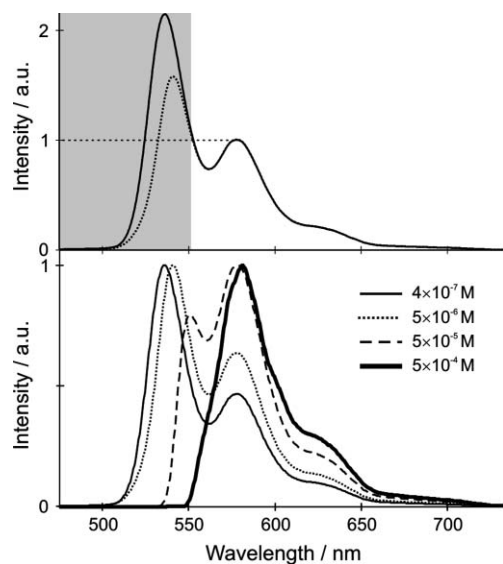


**Fig. 9** Distortion of the fluorescence spectrum caused by self-absorption. Top: fluorescence spectra of two DXP solutions,  $3.8 \times 10^{-7} \text{ mol L}^{-1}$  (solid) and  $5 \times 10^{-6} \text{ mol L}^{-1}$  (dotted), scaled to the same height at 577 nm where self-absorption does not affect the emission spectrum. The spectral distribution of the intensity is changed: the intensity of the short-wavelength region of the more concentrated solution is lower. Bottom: fluorescence spectrum of the  $4 \times 10^{-7} \text{ mol L}^{-1}$  DXP solution and simulated spectra of  $5 \times 10^{-7} \text{ mol L}^{-1}$ ,  $5 \times 10^{-5} \text{ mol L}^{-1}$  and  $5 \times 10^{-4} \text{ mol L}^{-1}$  solutions, scaled to the same peak height in the region where self-absorption affects the spectrum (here at the emission maxima). The red shift increases with increasing concentration, causing a considerable distortion of the original spectrum.

Together with the decrease of intensity in the spectral overlap region, self-absorption causes a red shift of the emission maximum. Fig. 9(bottom) shows the emission spectrum of the  $4 \times 10^{-7} \text{ mol L}^{-1}$  DXP solution and the simulated emission spectra of higher concentrations, namely  $5 \times 10^{-6} \text{ mol L}^{-1}$ ,  $5 \times 10^{-5} \text{ mol L}^{-1}$  and  $5 \times 10^{-4} \text{ mol L}^{-1}$ . The spectra are scaled to the same peak height of the emission maximum (where self-absorption takes place). We observe a considerable shift of the emission maximum. The higher the concentration, the larger is the shift.

#### 4. Sequential insertion of molecules

The fact that appropriately chosen molecules cannot glide past each other because the channels of zeolite L are too narrow can be used to realize sandwich-type materials in a manner as explained in Fig. 10. We have developed and used this for luminescent dyes because such materials can be analyzed in fluorescence microscopy experiments. The first step consists of inserting a certain amount of a dye1 by ion exchange or from the gas phase, depending on its properties. This leads to a material we name *dye1-zeolite L*. After removing dyes which might eventually be adsorbed at the outer surface, the dye2 is inserted. Conditions must be chosen such that dye1 has no chance to exit the channels at the beginning of this second step. Once a dye2 molecule has entered each channel on both sides, the dye1 molecules have no chance to escape anymore. On the contrary, they enter deeper into the channels, because the following dye2 species push them deeper in, and we recollect the *dye2,dye1-zeolite L* material. The same procedure is repeated for dye3. The resulting material is the *dye3,dye2,dye1-zeolite L* sandwich material. Different insertion methods can be combined. Dye1 can e.g. be a cationic dye. Hence, it is inserted by cation exchange. Dye2 can be a neutral dye, hence, we insert it from the gas phase and so on. Structures with more than three different dyes can be prepared if desired. Many materials of this kind have been prepared and characterized.<sup>27,40,65,66</sup>

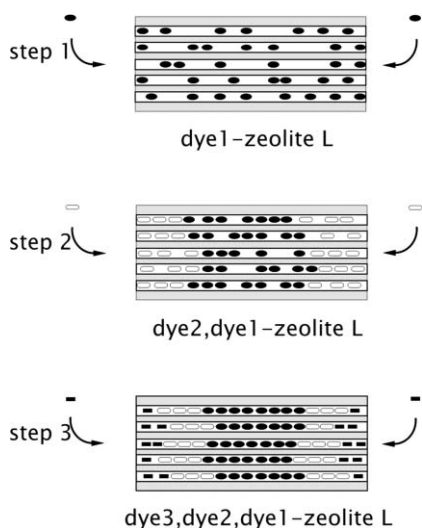


**Fig. 10** Sequential insertion step 1, step 2, and step 3 of three different dyes into the channels of a zeolite L crystal to form a sandwich material.

We show in Fig. 11 fluorescence microscopy images of single crystals, sequentially loaded with two dyes, Ox<sup>+</sup> and DMPOPOP, on the left, and with 3 dyes, Ox<sup>+</sup>, DMPOPOP and Py<sup>+</sup>, on the right. The orientation of the S<sub>1</sub> ↔ S<sub>0</sub>, π, π\* ETDM of Ox<sup>+</sup> shows a cone-shaped distribution with a half cone angle of 72° with respect to the channel axis while it is parallel for DMPOPOP.<sup>65</sup> Observing a DMPOPOP, Ox<sup>+</sup>-zeolite L crystals in a microscope equipped with polarizers, an appropriate set of filters and using an immersion lens one can see the images shown in Fig. 11 in the left column. The blue emission Fig. 11(A) is observed through a polarizer parallel to the cylinder axis when specifically exciting DMPOPOP at λ = 330–385 nm while the red emission Fig. 11(C) is seen when the

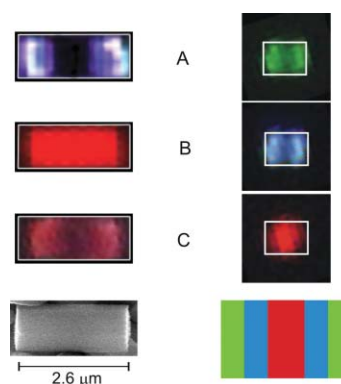


**Fig. 11** Fluorescence microscopy images of sandwich materials. Left: DMPOPOP, Ox<sup>+</sup>-zeolite L crystals. (A) The blue emission is observed through a polarizer parallel to the cylinder axis when specifically exciting DMPOPOP at λ = 330–385 nm. (C) The red emission C is seen when the polarizer is turned into vertical position. Image (B) is observed without polarizer upon excitation of Ox<sup>+</sup> at λ = 545–580 nm. On the bottom we show the SEM image of a crystal used in these experiments.<sup>65</sup> Right: Py<sup>+</sup>, DMPOPOP, Ox<sup>+</sup>-zeolite L crystals. The shape of the about 1.5 μm long zeolite L crystal we have used is indicated by the white rectangles. (A) To visualize the green Py<sup>+</sup> emission, the crystal was excited at 470–490 nm and the emission was detected through a broad band interference filter at 550 nm. (B) The blue DMPOPOP emission was recorded by exciting the DMPOPOP at 330–385 nm and observing the emission polarized in the direction of the crystal axis. (C) The red Ox<sup>+</sup> emission was detected after excitation at 545–580 nm. A scheme of the crystal build up is given at the bottom.<sup>27</sup>

polarizer is turned into vertical position. Image Fig. 11(B) is observed without polarizer upon excitation of Ox<sup>+</sup> at λ = 545–580. The shape of the crystal as seen by electron microscopy is shown on the bottom. These data show that the organization of the dyes inside the crystal corresponds to the situation obtained in step 2, Fig. 10. Image Fig. 11(C) also illustrates that energy transfer occurs from the DMPOPOP to the Ox<sup>+</sup>, an interpretation that is supported by time- and space resolved measurements.<sup>65</sup>

While the stacking of the dyes is visible in an optical microscope equipped with polarizer and appropriate optical filters for sufficiently large crystals, analysis of small crystals and correspondingly thin layers of the different dyes can be more delicate. We can stress the resolution limits of simple optical microscopy in favorable cases. This is illustrated in Fig. 11 in the right column, where we show fluorescence microscopy images of Py<sup>+</sup>, DMPOPOP, Ox<sup>+</sup>-zeolite L of about 1500 nm length. The middle of the crystal is filled with Ox<sup>+</sup>, followed by a thin layer of DMPOPOP, and on both ends we have Py<sup>+</sup>. Without taking care we would observe a mixture of all colors under the fluorescence microscope due to energy transfer from one dye to the other. We can examine the different regions of one single crystal as follows. After specific excitation of the Py<sup>+</sup> and detection through an interference filter around 550 nm one can clearly see the green Py<sup>+</sup> emission, Fig. 11(A). Using a polarizer one can, after selective DMPOPOP excitation, single out the blue DMPOPOP emission which is (unlike the Py<sup>+</sup> and Ox<sup>+</sup> emission) polarized along the crystal axis, Fig. 11(B). Finally, the red Ox<sup>+</sup> emission can be visualized by selectively exciting the Ox<sup>+</sup> molecules, Fig. 11(C).

## 5. Förster energy transfer experiments

In this section we present studies of Förster-type energy transfer in two systems: antenna materials and materials where donors and acceptors are randomly mixed inside the channels. We call the second type of material mixed-dye material. In the following experiments of mixed-dye and antenna materials, the donor–acceptor pair is the same,  $\text{Py}^+$  and  $\text{Ox}^+$ .

### 5.1. Mixed dye material

The energy transfer rate constant is strongly distance-dependent, eqn (3). The mean value of the rate constant can be obtained in a system where donor and acceptor molecules are randomly distributed inside the channels, while their ratio is 1 : 1. In such a system, the mean donor–acceptor distance can be controlled by varying the concentration of dyes.

$\text{Py}^+$  and  $\text{Ox}^+$  enter the zeolite channels at about the same speed providing a homogeneous distribution inside the channels. They are therefore a suitable donor–acceptor pair to realize this experiment,  $\text{Py}^+$  as donor and  $\text{Ox}^+$  as acceptor. Their excitation and emission spectra, after incorporation into zeolite L, are shown

in Fig. 12(B). The spectral overlap between the  $\text{Py}^+$  emission and the  $\text{Ox}^+$  absorption is marked in grey. This system allows beautiful visualization of energy transfer. Fig. 12(A) shows a photographic image of seven fluorescent samples.<sup>67</sup> Zeolite L crystals of 300 nm average length were filled as follows: The two references  $\text{Py}^+$  and  $\text{Ox}^+$  were loaded with  $5 \times 10^{-3}$  M of  $\text{Py}^+$  and  $5 \times 10^{-3}$  M of  $\text{Ox}^+$ , respectively. Samples A to E were filled with 1 : 1 random mixture of both dyes; we use the symbol  $p_{1/2}$  when describing them to express the fact, that the total dye loading is  $2 \cdot p_{1/2}$ . The corresponding concentrations are: A,  $2 \times (5 \times 10^{-4}$  M or  $p_{1/2} = 0.0014$ ); B,  $2 \times (1.25 \times 10^{-3}$  M or  $p_{1/2} = 0.0035$ ); C,  $2 \times (2.5 \times 10^{-3}$  M or  $p_{1/2} = 0.007$ ); D,  $2 \times (5.0 \times 10^{-3}$  M or  $p_{1/2} = 0.014$ ); E,  $2 \times (1.0 \times 10^{-2}$  M or  $p_{1/2} = 0.028$ ). From A to E the concentration of dyes increases, and hence the mean donor–acceptor distance decreases. Excitation was in all cases at 485 nm, where the absorption of  $\text{Py}^+$  is strong and that of  $\text{Ox}^+$  very weak as can be seen from the absorption spectra given in Fig. 12(B). We observe in sample A mainly the green fluorescence of  $\text{Py}^+$ , which indicates that energy transfer is insignificant, as schematically show by the crystal and the donor–acceptor pair on the left. But the yellow colour of sample B is due to a mixture of green and red fluorescence, which means that energy transfer is

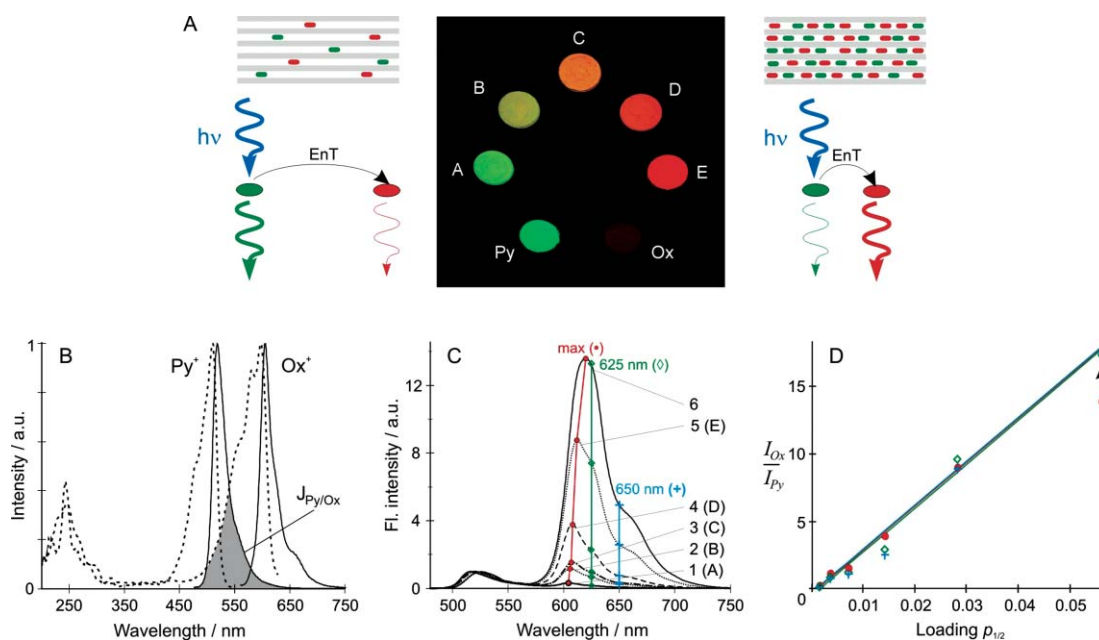


**Fig. 12** Visual demonstration of energy transfer. Middle: photographic image of the fluorescence of dye-loaded zeolite L layers upon monochromatic irradiation at 485 nm through an interference filter and observation through a 500 nm cut-off filter. The two samples indicated as  $\text{Py}^+$  and  $\text{Ox}^+$  are references loaded with pure  $\text{Py}^+$  and  $\text{Ox}^+$ , respectively. Samples A to E contain a 1 : 1 mixture of  $\text{Py}^+$  and  $\text{Ox}^+$  with the following loading for each dye: A,  $p_{1/2} = 0.0014$ ; B,  $p_{1/2} = 0.0035$ ; C,  $p_{1/2} = 0.007$ ; D,  $p_{1/2} = 0.014$ , and E,  $p_{1/2} = 0.028$ . Left: crystal and donor–acceptor pair describing the situation in sample A. The dye loading is low, hence, the donor–acceptor distance is large. When the donor is selectively excited, its fluorescence intensity is dominant (green light), while the energy transfer process to an acceptor is insignificant, and the acceptor fluorescence is very weak. Right: crystal and donor–acceptor pair describing the situation in sample E. High loading of the dyes results in a short donor–acceptor distance. The energy transfer process is very efficient. Fluorescence of the donor is weak, while fluorescence of the acceptor is strong. (B) Excitation (dashed) and fluorescence (solid) spectra of  $\text{Py}^+$  and  $\text{Ox}^+$  in zeolite L scaled to the same height at the maximum. (C) Fluorescence spectra (after excitation of  $\text{Py}^+$  at 450 nm, scaled to the same peak height of the  $\text{Py}^+$  emission at about 520 nm) of a series of six samples containing a 1 : 1 mixture of  $\text{Py}^+$  and  $\text{Ox}^+$  with the following loadings of each dye: 1,  $p_{1/2} = 0.0014$ ; 2,  $p_{1/2} = 0.0035$ ; 3,  $p_{1/2} = 0.007$ ; 4,  $p_{1/2} = 0.014$ ; 5,  $p_{1/2} = 0.028$  and 6,  $p_{1/2} = 0.056$ . The letters in brackets (A to E) indicate that these spectra correspond roughly to samples A to E in (A). (D) Acceptor to donor emission maxima ratio *versus* loading is linear for this system. The ratio is plotted at three acceptor wavelengths: the maximum of the emission (red line and (●)), 625 nm (green line and (◇)), and 650 nm (blue line and (+)). The points represent the experimental data and the lines were fitted according to eqn (9). The value of the emission maximum data of the sample with the highest loading,  $p_{1/2} = 0.056$ , is much lower due to self-absorption.<sup>67</sup>

significant in this sample. It becomes more and more important with increasing concentration so that from sample C on the red fluorescence stemming from  $\text{Ox}^+$  is dominant.

It is possible to do measurements over a larger concentration range than reported in Fig. 12(A). However, considerable self-absorption occurs due to the very high absorptivity of the individual crystals. Results of measurements scanning a larger concentration range, namely from  $2 \times (10^{-4} \text{ mol L}^{-1})$  up to  $2 \times (0.021 \text{ mol L}^{-1})$ , which corresponds to  $p_{1/2} = 0.0014$  up to  $p_{1/2} = 0.056$ , are reported in Fig. 12(C)–(D). In this case, zeolite L crystals of 700 nm average length were used. The emission spectra of the samples were recorded upon selective excitation of the donor (450 nm) and scaled to the same peak height of the  $\text{Py}^+$  emission. One can see that energy transfer becomes more efficient with increasing loading, as the emission of  $\text{Ox}^+$  becomes more intense.

The ratio of the fluorescence intensities acceptor ( $I_{\text{Ox}}$ ) to donor ( $I_{\text{Py}}$ ) depends linearly on the loading

$$\frac{I_{\text{Ox}}}{I_{\text{Py}}} = Cp_{1/2} \quad (9)$$

where  $C$  is a constant. Plotting the ratio of intensities *versus* loading at three acceptor wavelengths, namely the maximum of the emission, 625 nm, and 650 nm, we obtain the result presented in Fig. 12(D). We observe that the 625 nm and 650 nm data follow eqn (9) well, while when plotting the emission maximum data the last point is much too low. The reason for this is that the fluorescence spectrum of  $\text{Ox}^+$  is not affected at 625 nm and 650 nm by the self-absorption process while it is at shorter wavelengths. Self-absorption also causes a red shift of the emission maximum, as can be very well seen in the spectrum of sample 6. The mean value of the energy transfer rate constant ( $k_{\text{EnT}}$ ) of the mixed dye system can be estimated as described in ref. 67,68. For a fully loaded crystal ( $p_{1/2} = 0.5$ ) we found a value of  $k_{\text{EnT}}$  in the order of  $5 \times 10^{10} \text{ s}^{-1}$ , which reflects the high energy transfer efficiency in this system.

The fluorescence dynamics of the donor in the mixed dye system shows the following *stretched-exponential* behaviour<sup>10,69</sup>

$$I_{\text{D}}(t) = e^{-\frac{t}{\tau_{0,\text{D}}}} e^{-2\gamma\left(\frac{t}{\tau_{0,\text{D}}}\right)^\delta} \quad (10)$$

where  $\tau_{0,\text{D}}$  is the decay time of the donor in absence of energy transfer,  $\gamma$  is the parameter related to acceptor concentration and  $\delta$  is the dimensionality parameter.  $\delta$  is equal to 1/2, 1/3 and 1/6 for 3D, 2D and 1D, respectively. We observed that  $\delta$  decreases with increasing loading, Table 3, which means a decrease of energy transfer dimensionality.<sup>67</sup> This phenomenon comes from the anisotropy of the host which does not much influence the systems behaviour at low loading, this means that the energy transfer steps happen along and between the channels with

**Table 3** Parameter of dimensionality  $\delta$  at different values of loading  $p_{1/2}$

Sample	Loading $p_{1/2}$	$\delta$
1	0.0014	0.459
2	0.0035	0.395
3	0.007	0.353
4	0.014	0.337
5	0.025	0.218
6	0.056	0.229

similar probability; the value of  $\delta$  is close to 1/2. The influence of geometrical constraints of the host increases, however, with increasing loading. Energy transfer steps happen more and more preferentially along the channels and less and less between them. Only sample 6 deviates because of self-absorption, which also influences the luminescence decay. The energy transfer anisotropy is an interesting feature of these dye–zeolite L materials.

## 5.2. Antenna materials

Antenna systems are supramolecular arrangements in which electronic excitation of molecules occurs in a given volume and in which the electronic excitation energy is then transported by a radiationless process (near-field interactions) to a well-defined location. Sequential insertion of dyes in channels, as discussed in Section 4, has been shown to be an excellent tool for preparing such systems. We now discuss observations on energy transfer in antenna materials and the dependence of the energy transfer efficiency on some parameters.

Fig. 13(A) shows a schematic representation of an individual crystal of an antenna material. The crystal is filled with donor molecules in the middle, while the channel ends are occupied by acceptors. Energy is transported in two directions towards channel ends; we therefore call this material *bidirectional antenna*. If one of the green dyes is electronically excited, the excitation energy can travel randomly, until it is lost by spontaneous emission or captured by one of the red acceptors and then released by them as fluorescence. Fig. 13(B) shows a fluorescence microscopy image of such material upon excitation of only green emitting molecules. We see the green emission of donors in the middle part of the crystals and a yellow emission at the channel ends. This yellow color results from the superposition of green and red emission of donors and acceptors, respectively. The confocal microscopy images of similar material with relatively large crystals in Fig. 13(C)–(D) show nicely that the dyes are really situated as proposed by the schematic representation in Fig. 13(A).<sup>70</sup> We observe the green donor fluorescence in the middle part of the crystal upon selective excitation of the donor and applying an optical filter, Fig. 13(C). Selectively exciting acceptors results in their red fluorescence at both crystal ends, Fig. 13(D).

Time-resolved investigations upon selective excitation of the donors show the behavior one would expect for Förster energy transfer. The donor intensity dynamics is shown in Fig. 13(E). The intensity decay in presence of acceptors is shown as solid line; it is faster than the decay in absence of acceptors (dotted line), as energy transfer is an additional process depopulating the excited state of the donor. The intensity dynamics of the acceptors is shown in Fig. 13(F). It rises first before it starts to decay. The reason is that the acceptors are not excited directly but are “pumped” to the excited state *via* energy transfer. The more efficient the energy transfer, the faster is the rise, which is often difficult to be observed for molecules with a luminescence lifetime of only a few ns. This rise has been very nicely observed in the antenna materials<sup>70</sup> and also in the mixed dye material.<sup>67</sup>

The efficiency of Förster energy transfer, *i.e.* the efficiency of electronic excitation delivery to acceptors, depends on two parameters: the loading of donors and the length of the crystal. The energy transfer efficiency is low for low donor loading and for long crystals. Experiments made with samples of different

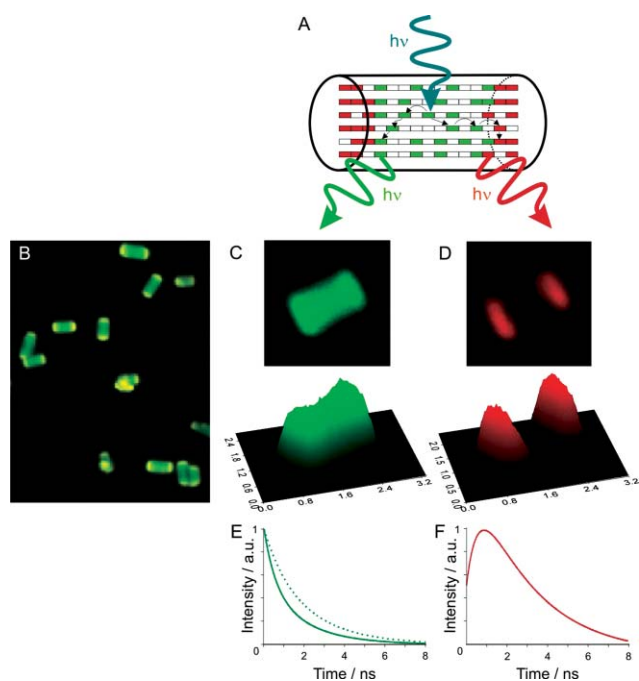


**Fig. 13** Fluorescence behaviour of an  $\text{Ox}^+$ ,  $\text{Py}^+$ -zeolite L antenna. (A) Scheme of an antenna crystal and processes taking place upon excitation of a donor molecule: absorption of incident light, energy migration from an excited donor molecule to a neighboring unexcited one and trapping by an acceptor (black arrows), fluorescence of both donor and acceptor. (B) Fluorescence microscopy image of such antenna crystals upon selective excitation of donors. The yellow color at the channel ends is due to a mixture of green donor and red acceptor emission. (C) Confocal microscopy images of an antenna crystal upon selective excitation of the donor and observation through an appropriate filter. (D) Confocal microscopy images upon selective excitation of the acceptor. (E) and (F) Time-resolved intensity dynamics of the donor (E) and the acceptor (F) upon selective excitation of the donor. (E) Donor fluorescence dynamics in absence (dotted) and in presence (solid) of acceptors. The faster decay in presence of acceptors indicates energy transfer taking place. (F) Acceptor intensity dynamics. The rise of intensity reflects the “pumping” of acceptors through energy transfer.<sup>70</sup>

donor loading are presented in Fig. 14(A)–(B). The average length of the crystals is the same (600 nm), as well as the loading of acceptors, two  $\text{Ox}^+$  molecules at each channel end on average. The donor loading  $p_{\text{Py}}$  increases from sample 1 to 6 as follows: 1, 0.007; 2, 0.012; 3, 0.031; 4, 0.057; 5, 0.106; 6, 0.182. The fluorescence spectra observed after specific excitation of  $\text{Py}^+$  at 470 nm are scaled to the same height at the maximum of the  $\text{Py}^+$  emission at about 520 nm. The energy transfer efficiency, and hence the  $\text{Ox}^+$  emission intensity, increases with increasing donor loading. The reason for this is that the mean distance between the molecules becomes shorter which causes an increase of the energy transfer rate constant, according to eqn (3). This means that the probability for electronic excitation to reach neighboring molecule before decaying increases. The ratio of the acceptor to donor intensities *versus* donor loading  $p_{\text{Py}}$  is presented in Fig. 14(B). The points are connected with a line for better visualization. Comparing these results with those in Fig. 12(D) for mixed dye material, we observe that the energy transfer efficiency in antenna materials increases faster, non-linearly, with donor loading than in mixed dye material where a linear dependence on donor loading

is observed. We assume that the reason for this different behavior is the influence of the staggered profile of the donor and acceptor inter-phases which will be discussed in more detail in the next section. Due to this there are always some favourable molecule arrangements where donor and acceptor are close so that energy transfer is very efficient. At low loadings these favourable cases considerably increase the mean energy transfer rate constant.

Fig. 14(C)–(D) show results of experiments where the donor-loading is constant,  $p_{\text{Py}} = 0.11$ , while the average crystal length varies: 1, 300 nm; 2, 500 nm; 3, 850 nm; 4, 1400 nm; 5, 2400 nm.<sup>36</sup> The channel ends of all crystals were modified with two  $\text{Ox}^+$  molecules on average. The fluorescence spectra after specific excitation of  $\text{Py}^+$  at 460 nm are scaled to the same height at the maximum of the  $\text{Py}^+$  emission at about 520 nm. A strong increase of energy transfer efficiency with decreasing crystal length is observed. The efficiency of individual energy migration steps in short and in long crystals is the same, because of equal donor loading. In a short crystal, however, fewer steps are needed to reach an acceptor. The probability for an excitation to reach an acceptor is therefore higher, as there is less time to find a non-luminescent trap, to decay radiationlessly or to emit spontaneously. About 90% of the emitted light is due to energy migration along the  $\text{Py}^+$  and transfer to the luminescent traps  $\text{Ox}^+$  in the 300 nm crystals.<sup>36</sup> This result is to be expected if Förster energy transfer is the main process. There is a small red shift of  $\text{Py}^+$  emission with increasing  $\text{Py}^+$  loading and with increasing length of the crystals, respectively, in both experiments. It is caused by the self-absorption due to increased absorptivity of individual crystals which increases with loading and with size.

## 6. Increasing organization

Anisotropic functionality and a high degree of supramolecular organization are important for attaining specific microscopic and eventually also macroscopic properties. We now show that low dimensionality and an impressive level of organization can be achieved in dye-loaded zeolite L crystals.

### 6.1. 1D energy migration

An important question concerns the dimensionality of the near-field interaction driven excitation energy transport. Decrease of dimensionality with increasing loading has been discussed in the previous section. To further investigate this, we prepared zeolite L crystals schematically presented in Fig. 15(A), where we have red acceptor molecules in the middle followed by blue spacers and green-emitting donors. The idea behind this experiment was to investigate the distance dependence of the energy transfer probability from donors to acceptors for varying thickness  $R$  of the spacer layer. To prepare this material, crystals were first loaded with acceptors ( $\text{Ox}^+$ ), then with spacers (DMPOPOP), and finally with the donors ( $\text{Py}^+$ ). The excitation and fluorescence spectra of the individual dyes are shown in Fig. 15(C), excitation spectra as dotted lines and fluorescence spectra as solid ones. Upon specific excitation of  $\text{Py}^+$ , as indicated by the arrow, DMPOPOP does not absorb light at this wavelength and hence does not participate in the energy transfer process, it only spatially separates  $\text{Py}^+$  and  $\text{Ox}^+$ . Fig. 15(D) shows the fluorescence spectra of the resulting materials upon excitation as indicated by the arrow in Fig. 15(C).

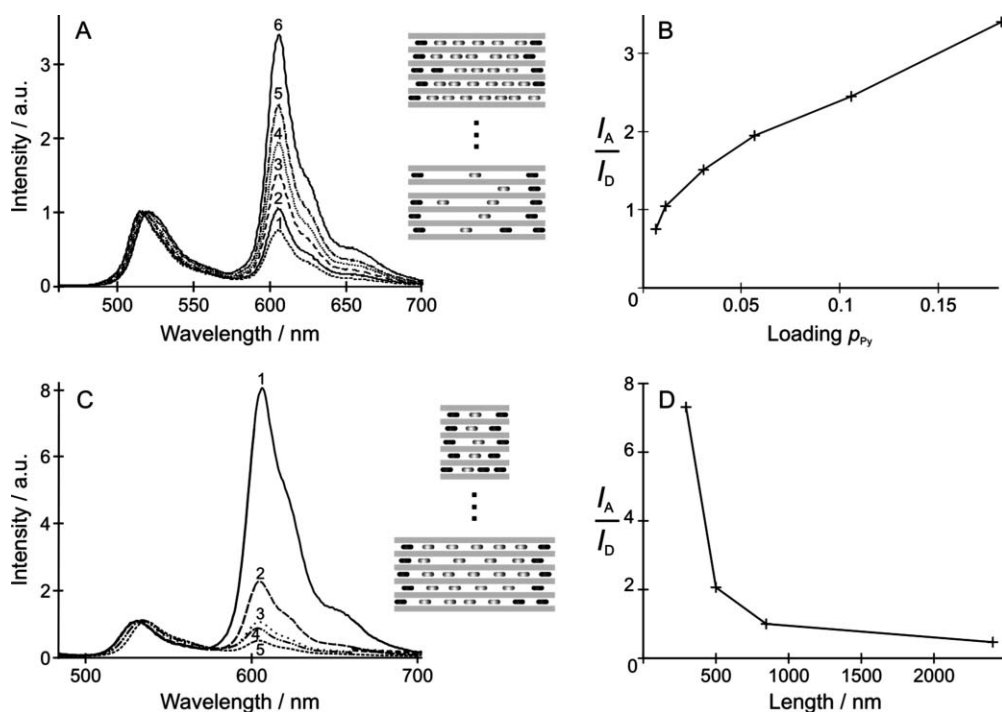


**Fig. 14** Dependence of energy transfer efficiency on donor loading and crystals length. (A) and (B): Experiments with different donor loading. Crystal length and acceptor (dark rectangles) loading were kept constant, while donor (grey rectangles) loading  $p_{Py}$  varied: 1, 0.007; 2, 0.012; 3, 0.031; 4, 0.057; 5, 0.106; 6, 0.182. (A) Fluorescence spectra upon excitation of  $Py^+$  at 470 nm. The energy transfer efficiency increases with increasing donor loading. (B) Acceptor to donor emission maxima ratio plotted *versus*  $p_{Py}$ . (C) and (D): Experiment with different crystal length. The loading of donors was kept constant,  $p_{Py} = 0.11$ , and all samples were modified with two acceptor molecules at each channel end on average, while the crystal length varied: 1, 300 nm; 2, 500 nm; 3, 850 nm; 4, 1400 nm; 5, 2400 nm. (C) Fluorescence spectra upon excitation of  $Py^+$  at 460 nm. The energy transfer efficiency decreases with increasing crystal length. (D) Acceptor to donor emission maxima ratio plotted *versus* crystal length.

The numbers 8.5, 11, 16 and 22.5 indicate the average number  $n$  of DMPOPOP molecules in the spacer layer. As one can see, the amount of energy transferred to the acceptor decreases with increasing thickness of the spacer layer. This clearly indicates that the process is controlled by near-field interaction.

The distance dependence of the probability  $P$  for Förster-type energy transfer from an electronically excited donor to an acceptor can be expressed as follows

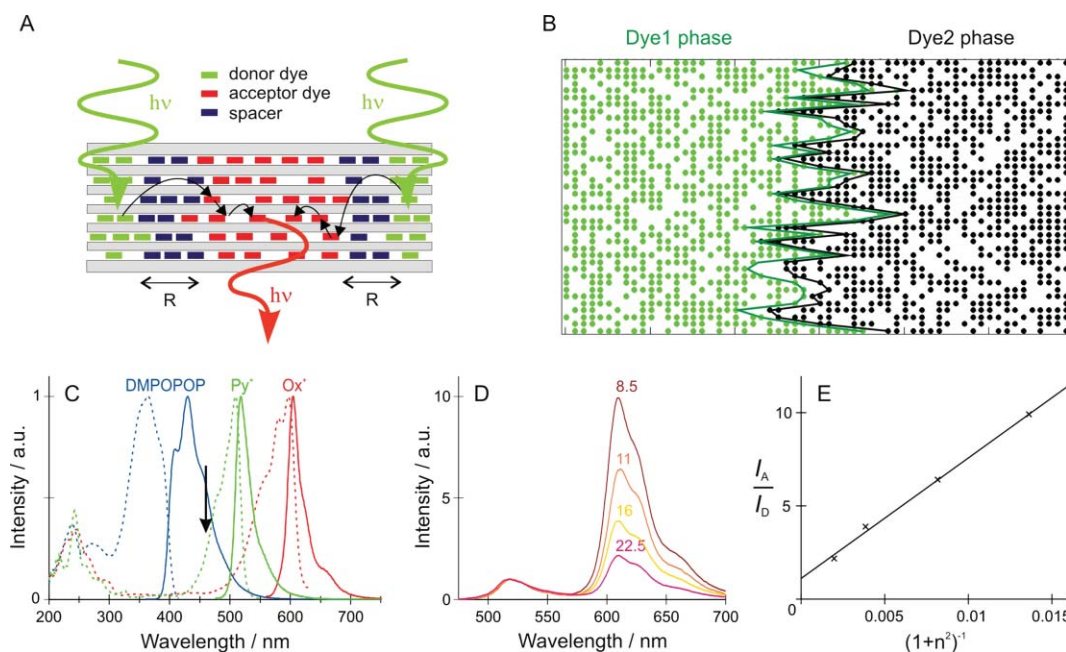
$$P = \frac{1}{1 + (R_{DA}/R_0)^a} \quad (11)$$

where  $R_0$  is the Förster radius, which is the distance at which the energy transfer probability is 50%, and  $a$  is the parameter of dimensionality, equal to 6, 4 and 2 for 3D, 2D and 1D systems, respectively. We do not have access to the mean value of the donor–acceptor distance  $R_{DA}$ . However, the average number  $n$  of spacer molecules is proportional to this distance. Therefore, the acceptor fluorescence intensity was plotted *versus*  $1/(1 + n^a)$ , and it was found that the data obey an  $a = 2$  behaviour which is characteristics for a 1D transport, see Fig. 15(E). In the case of dye–zeolite L materials, however, it is more correct to use the term “*quasi-1D energy transfer*”: the statistical mean of energy transfer is directed along the  $c$ -axis of the crystal, but individual energy transfer steps can also occur to a neighbouring channel. This result is probably the first experimental proof given in the literature for quasi 1D electronic excitation energy transport.<sup>66</sup>

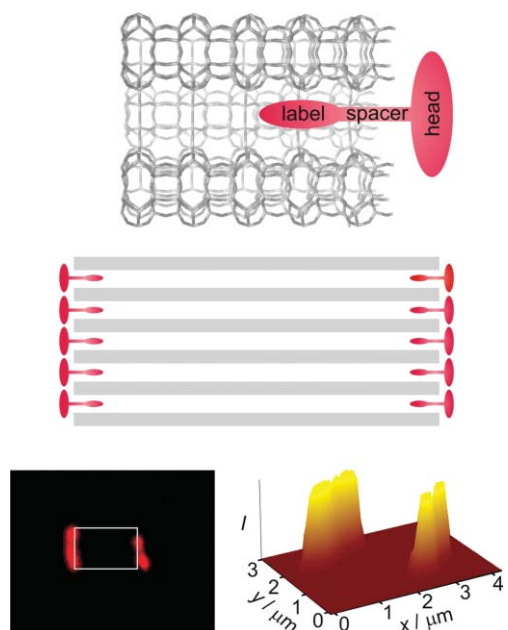
The mean distance  $R_{DA}$  cannot be obtained by simply multiplying the number of spacer molecules by their length, because of the staggered profile of the phase boundaries of dyes. Fig. 15(B) shows the phase boundary of Dye1 and Dye2 obtained by Monte-Carlo simulation.<sup>66</sup> We see that the phases of Dye1 and Dye2 overlap in the neighboring channels, and this overlap may extend over several sites. In this case the distance between the Dye1 and the Dye2 molecules situated in neighboring channels may become shorter than that between neighboring molecules in the same channel.

## 6.2. Stopcock principle

To realize communication of the dyes inside the zeolite channels with the outside world, a next organizational step is needed. What we did was to invent nano-stopcocks.<sup>71</sup> These are molecules that consist in principle of a label, a spacer and a head as shown in Fig. 16(top). The head of these molecules is too large to enter the channels. Since stopcock molecules are located at the interface between the interior of a zeolite L crystal and the surroundings, they can be considered as mediators for communication between dye molecules inside the nanochannels and objects outside of the crystals. Fluorescent stopcocks can be used to extract or inject electronic excitation energy into or from the zeolite L crystals by means of energy transfer. Stopcock molecules can also prevent penetration of small molecules such as oxygen and water or hinder encapsulated molecules, cluster and cations from leaving the channels.<sup>45</sup>



**Fig. 15** Dimensionality of energy transfer. (A) Scheme of an individual crystal of the material used for the experiment. Channels containing red-emitting dyes in the middle, followed by spacer layers of different average thickness (blue-emitting molecules), and finally green-emitting molecules at the ends. (B) Phase boundary of dyes. Image of a zeolite L crystal consisting of 40 channels, each containing 32 sites, as obtained by a Monte-Carlo simulation. The sites were first randomly filled with black dye molecules and then, after virtually sealing the right channel entrances, with green dye molecules (from the left side). The total dye loading is 0.6. The calculation indicates that the phase boundary extends over about 10 sites. (C) Excitation (dotted) and emission (solid) spectra of the applied dye molecules. The arrow indicates the excitation wavelength used for the experiment. (D) Fluorescence spectra scaled to the same peak height of the  $\text{Py}^+$  emission upon selective excitation (arrow in (C)). The numbers correspond to the average number of spacer molecules per spacer layer. (E) Intensity  $I_{\text{rel}}$  of the acceptor versus  $1/(1+n^2)$ , where  $n$  is the averaged number of spacer molecules confirming the value of  $a = 2$ .

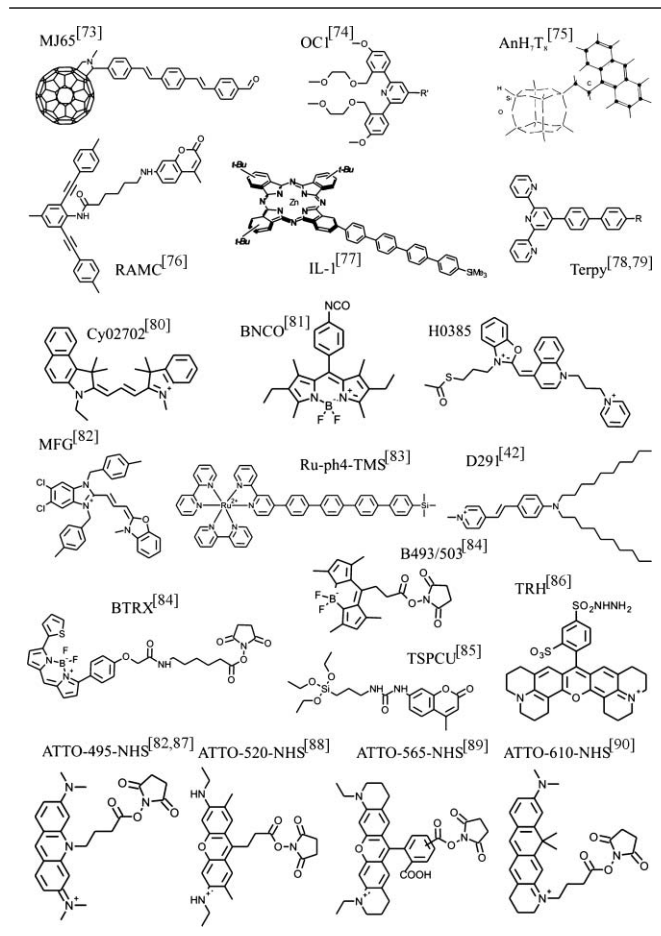


**Fig. 16** Stopcock principle. Top: one channel entrance with a schematically represented stopcock molecule. Middle: schematic representation of a zeolite crystal plugged with stopcock molecules at the channel entrances. Bottom: confocal fluorescence microscopy images of an ATTO-680-zeolite L crystal. The image indicates that only the base of the crystal is modified with ATTO-680.

Imagine a 600 nm diameter zeolite L crystal, and *that* you want to close each channel with a stopcock as schematically shown in Fig. 16(middle)—this would mean adding roughly 200 000 stopcocks. It is clear that such a problem is best solved by chemical means, which is by methods dealing with a large number of objects, and not by a physical approach which would address one channel opening after the other. Depending on the type, stopcocks can be bound either by physisorption, by electrostatic interaction, by covalent bonding or by a combination of electrostatic and covalent bonding. A selection of stopcocks successfully used so far is summarised in Table 4.

The best way to find out if and where the molecules are attached to a crystal is fluorescence microscopy—if possible in confocal mode—on crystals of different size. Fig. 16(bottom) shows as an example ATTO-680 covalently attached to both ends of a zeolite L crystal.<sup>72</sup> The red luminescence on both crystal bases comes from the attached ATTO-680. The zeolite crystal is marked with a rectangle in the image on the left side.

An example of stopcock molecule blocking the channel entrance is octasilasesquioxane ( $\text{H}_7\text{Si}_8\text{O}_{12}$ ) with an anthracene head, indicated as  $\text{AnH}_7\text{T}_8$  in Table 4. We show in Fig. 17(A) a van der Waals model of this molecule and part of the channel entrance. The  $\text{H}_7\text{Si}_8\text{O}_{12}$  head fits tightly into the channel, sealing it completely, while the anthracene part, which is seen by its blue luminescence in Fig 17(B), remains at the outside. This interpretation is supported by the observation, that  $\text{AnH}_7\text{T}_8$  plugged zeolite L crystals tend to form chains as seen in the fluorescence microscopy image Fig. 17(C), the driving force being van der Waals interactions

**Table 4** Examples of stopcock molecules

between the anthracene parts. The white rectangles mark the crystals, and the fluorescence at the crystal edges stems from the anthracene heads.

### 6.3. Stopcock-plugged antenna

*Stopcock-plugged antenna* are dye loaded zeolite crystals where either the donors or the acceptors are stopcock molecules. Our very early success in making a stopcock-plugged antenna material was by first filling zeolite L with the red-luminescent  $\text{Ox}^+$  (acceptor) and then modifying the channel entrances with the green B493/503 stopcock (donor) as shown in Fig. 18(A).<sup>84</sup> The excitation and emission spectra of both dyes are shown in Fig. 18(B). Excitation of the B493/503,  $\text{Ox}^+$ -zeolite L sample at  $21740\text{ cm}^{-1}$  leads to a considerable fluorescence of  $\text{Ox}^+$ , Fig. 18(C), proving that energy transfer from the stopcock to the acceptor inside the channels takes place. In this system energy is transported from the outside of the crystal to the acceptor molecules inside.

In the next experiment we realized transfer of excitation energy in the reverse direction, from the inside to the outside of the crystal. This was achieved with the blue-emitting  $\text{MC}^+$  as donor and the green-emitting stopcock MFG as acceptor.<sup>87</sup> The excitation and emission spectra recorded in this experiment are shown in Fig. 18(E). The fluorescence spectrum of the MFG,  $\text{MC}^+$ -zeolite L sample upon selective excitation of  $\text{MC}^+$  shown in Fig. 18(F) proves that energy transfer from the molecules inside to the

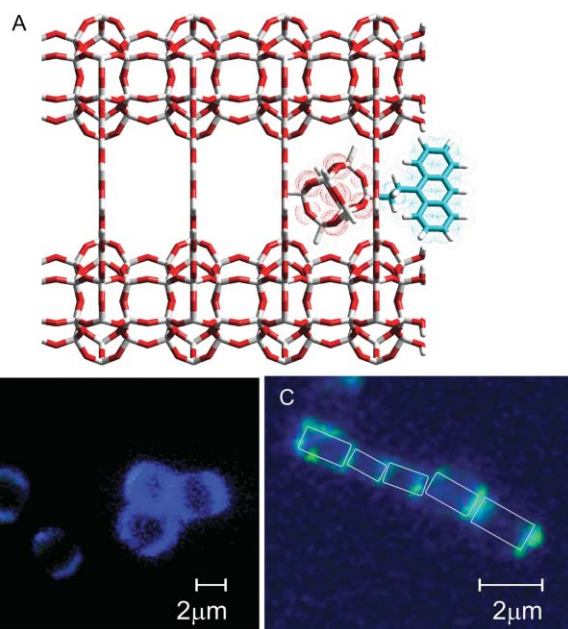


**Fig. 17** Stopcock  $\text{AnH}_7\text{T}_8$ :  $\text{H}_7\text{Si}_8\text{O}_{12}$ -label and anthracene-head. (A) van der Waals model of the molecule and entrance of a zeolite L channel. The molecule fully blocks the channel entrance. (B) Fluorescence microscopy images of some  $\text{AnH}_7\text{T}_8$ -zeolite L crystals. (C) Chain of five  $\text{AnH}_7\text{T}_8$ -zeolite L crystals.<sup>75</sup>

stopcock molecules takes place. These examples demonstrate that both directions of energy transfer by near field interaction are possible: from the outside of the crystal to the inside, and reverse, from the inside of the crystal to the outside.

The  $\text{Ru}^{2+}$  complex (Ru-ph4-TMS) has a tail which nicely fits into the channel. The head is positively charged and can therefore bind electrostatically to the negatively charged channel entrance as explained by means of Fig. 19(top). The van der Waals model of Ru-ph4-TMS shown in Fig. 19, indicates that the size of the head is such that it should be possible to plug the channels quantitatively.

Ru-ph4-TMS is a triplet emitter, and, as many other long lived species, is quenched by dioxygen *via* a diffusion controlled collision.<sup>91–93</sup> We have observed that the luminescence quenching of the Ru-ph4-TMS stopcock by  $\text{O}_2$  is much weaker when the former is bound to zeolite L, and we found that this is due to the delocalization of the emitting  $^3\text{MLCT}$  state over the bpy-ph4 ligand shielded by the zeolite L, which hinders the  $\text{O}_2$  in making successful collisions.<sup>94</sup> An even larger shielding effect was observed when the Ru-ph4-TMS stopcocks were attached to a zeolite L monolayer. The luminescence lifetime of the attached Ru-ph4-TMS stopcock was measured to be nearly the same under  $\text{O}_2$  and under  $\text{N}_2$  atmosphere.<sup>95</sup> We show emission spectra of the (Ru-ph4-TMS)-zeolite L monolayer in  $\text{N}_2$  and in  $\text{O}_2$  atmosphere in Fig. 20. The time delay between the curves shown is 200 ns. The great similarity between both emission spectra is remarkable. The lifetime in  $\text{O}_2$  and in  $\text{N}_2$  atmosphere is in the same order of magnitude as that of the free complex in solution under  $\text{N}_2$  atmosphere ( $\tau = 1207\text{ ns}$ ). This means that the zeolite host provides an excellent shielding of the emitting  $^3\text{MLCT}$  state of Ru-ph4-TMS, preventing collisions between the  $\text{O}_2$  quencher and the stopcock.

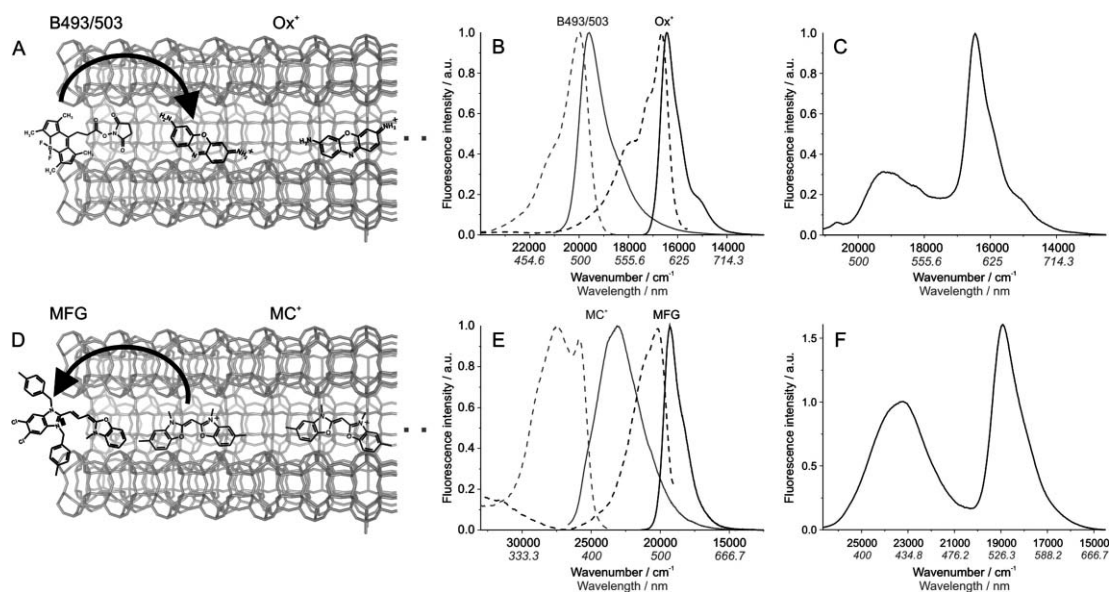


**Fig. 18** Energy transfer from outside of the crystal to the inside (top) and in the opposite direction (bottom). (A) Channel of a B493/503,  $\text{Ox}^+$ -zeolite L crystal, where electronic excitation energy is injected from the outside to the inside of the crystal. (B) Excitation (dashed) and emission (solid) spectra of B493/503-zeolite L and  $\text{Ox}^+$ -zeolite L. (C) Fluorescence spectra of the B493/503,  $\text{Ox}^+$ -zeolite L stopcock-plugged antenna material upon selective excitation of B493/503 at  $21740\text{ cm}^{-1}$ .<sup>84</sup> (D) Channel of the MFG,  $\text{MC}^+$ -zeolite L crystal, where electronic excitation energy is transported from the inside to the outside of the crystal. (E) Excitation (dashed) and emission (solid) spectra of MFG-zeolite L and  $\text{MC}^+$ -zeolite L. (F) Fluorescence spectra of the MFG,  $\text{MC}^+$ -zeolite L stopcock-plugged antenna material upon selective excitation of  $\text{MC}^+$  at  $28570\text{ cm}^{-1}$ .<sup>87</sup>

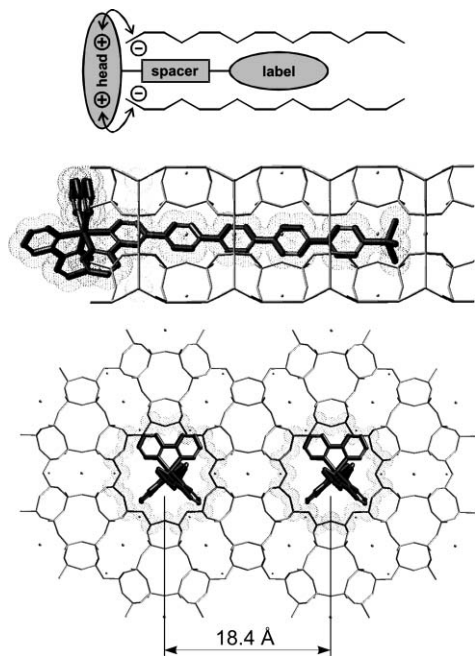


**Fig. 19** (Ru-ph4-TMS)-zeolite L material. Top: electrostatic binding of positively charged stopcock molecule to the negatively charged zeolite L channel entrance. Middle and bottom: structure of the (Ru-ph4-TMS)-zeolite L assembly. Side view (middle) shows that the tail is protected by the zeolite channel. Top view (bottom) illustrates the space needed for the stopcocks to arrange properly.

If the channels are filled with  $\text{Ox}1^+$ , before adding Ru-ph4-TMS, we obtain a stopcock-plugged material where energy is

transferred from the outside of the crystal to the inside. Fig. 21(top) shows excitation and emission spectra of (Ru-ph4-TMS)-zeolite L and  $\text{Ox}1^+$ -zeolite L, and Fig. 21(bottom) shows the luminescence spectrum of the (Ru-ph4-TMS),  $\text{Ox}1^+$ -zeolite L antenna material upon excitation of Ru-ph4-TMS.<sup>83</sup> Energy transfer is almost quantitative in this case; the emission of Ru-ph4-TMS with the maximum at 610 nm is quenched so strongly that it appears only as a weak shoulder. In another experiment, an oriented monolayer was prepared from  $\text{Ox}1^+$ -loaded zeolite L crystals that were afterwards modified with Ru-ph4-TMS stopcocks. The aim of the experiment was to see, whether a unidirectional energy transfer between the dye and the stopcock could be realised in a monolayer system. The luminescence spectra show very nicely that energy transfer from Ru-ph4-TMS to  $\text{Ox}1^+$  takes also place in this type of system.<sup>80</sup>

#### 6.4. More complex systems

We explain two principles to obtain materials that could be used for obtaining white light emitting materials. One is to incorporate three different well matching dye molecules into one zeolite L crystal, one of them being a stopcock. The other is to incorporate a stopcock plugged antenna material into a luminescent polymer. An example of the first one has been realized as follows: the channels were first filled with green emitting NY43, then with red emitting  $\text{Ox}^+$  and at the end the channel entrances were plugged with deep-red emitting ATTO-680 as shown in Fig. 22(top).<sup>96</sup> The excitation and emission spectra of the dyes are shown in Fig. 22(middle). Upon excitation of NY43, energy is transferred to  $\text{Ox}^+$ , and from  $\text{Ox}^+$  further to ATTO-680. Emission of all three dyes is observed as illustrated in the fluorescence spectrum,

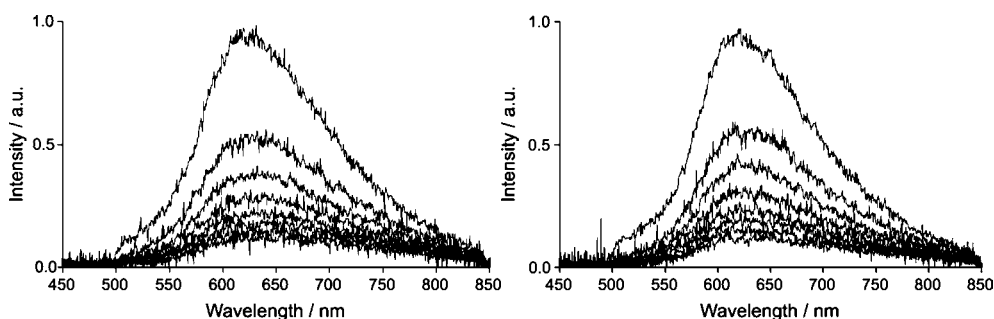


**Fig. 20** Time-resolved emission spectra of a (Ru-ph4-TMS)-zeolite L monolayer in toluene under O<sub>2</sub> (left) and under N<sub>2</sub> (right) atmosphere. The spectra were recorded at room temperature under excitation at 460 nm. The delay increment between consecutive spectra is 200 ns.<sup>95</sup>

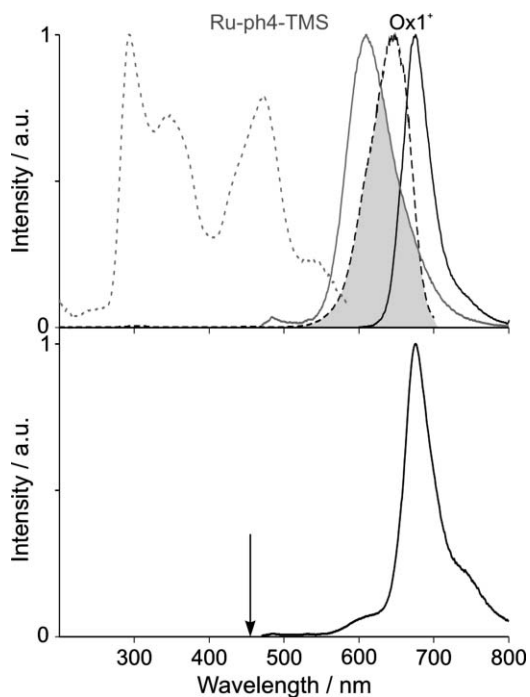


**Fig. 21** (Ru-ph4-TMS),Ox1<sup>+</sup>-zeolite L stopcock-plugged antenna material. Top: excitation (dashed) and emission (solid) spectra of (Ru-ph4-TMS)-zeolite L and Ox1<sup>+</sup>-zeolite L. The spectral overlap of the Ru<sup>2+</sup> emission and Ox1<sup>+</sup> absorption is shaded. Bottom: fluorescence spectrum of the stopcock-plugged antenna material upon excitation at 460 nm (indicated by the arrow). The shoulder at 610 nm is the remaining weak emission of Ru<sup>2+</sup> complex.<sup>83</sup>

Fig. 22(bottom). In the excitation spectrum measured at 725 nm, the bands of NY43 and Ox<sup>+</sup> are intense and that of the stopcock ATTO-680 is weak because its amount is low. The presented example is not an exception; similar systems can be prepared in many different ways.

Another way to obtain three colors in emission is *coupling of stopcock-plugged antenna crystals with a polymer*, so that energy injection from the polymer *via* stopcock to guest molecules takes place as explained in Fig. 23(A). In the example presented, not only the channel entrances but the whole external surface of the crystals was covered with stopcock molecules.<sup>82,87</sup> This was done as follows: the surface of Ox<sup>+</sup>-zeolite nanocrystals was modified with amino groups through siloxane linkages and then reacted

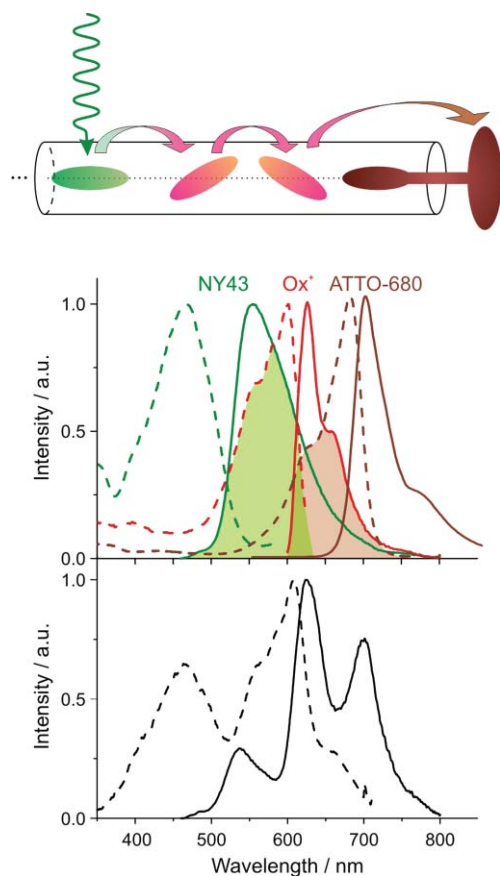


**Fig. 22** Stopcock-plugged antenna material with three kind of dyes, ATTO-680,Ox<sup>+</sup>,NY43-zeolite L. Top: a channel ending of the material. NY43 is excited, energy is transferred to Ox<sup>+</sup>, and then from Ox<sup>+</sup> to ATTO-680. Middle: excitation (dashed) and emission (solid) spectra of NY43-zeolite L (green), Ox<sup>+</sup>-zeolite L (red) and ATTO-680-zeolite L (deep red). Bottom: excitation spectra upon observation at 725 nm (dashed) and emission spectra upon excitation at 450 nm (solid) of the material. In the emission spectrum, bands of all three dyes are observed.

with ATTO-495-NHS, as shown in Fig. 23(C). The succinimidyl ester of the stopcock (see Table 4) is able to react with the amino groups on the modified crystal surface, yielding peptide linkages. The luminescent polymer in which the dye-zeolite crystals were embedded was poly(*N*-vinylcarbazole), shortly PVK; its structure

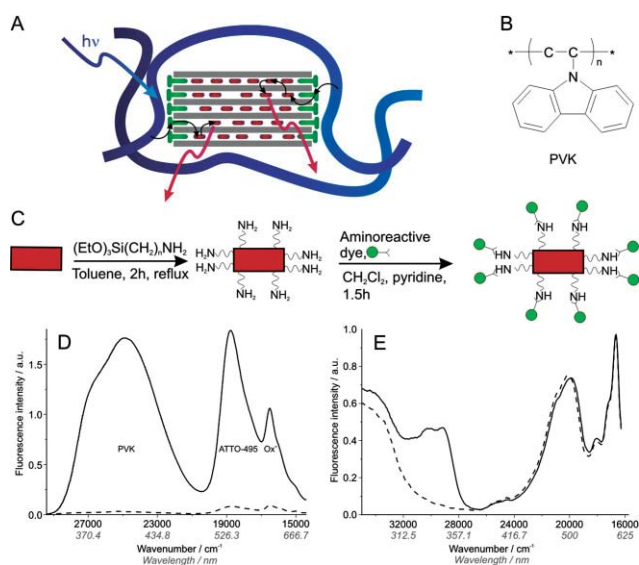


**Fig. 23** Coupling of stopcock-plugged dye-zeolite L antenna crystal with a luminescent polymer. (A) Scheme of the system. Upon excitation of the polymer, energy is transferred to a stopcock and from there further to guest molecules. The polymer is drawn as a blue ribbon. (B) Structure of PVK. (C) Modifying the whole crystal surface with a reactive dye (stopcock molecule). (D) Fluorescence spectra of ATTO-495,  $\text{Ox}^+$ -zeolite L embedded in PVK (solid) and of ATTO-495,  $\text{Ox}^+$ -zeolite L sample (dashed). Both samples contained an equal amount of ATTO-495,  $\text{Ox}^+$ -zeolite L and were excited at  $30\,300\text{ cm}^{-1}$ . Bands of ATTO-495 and of  $\text{Ox}^+$  are very small in the sample without polymer, while they are intense in the sample with polymer. (E) Excitation spectra of both samples upon detection at  $16\,260\text{ cm}^{-1}$ .<sup>82</sup>

is shown in Fig. 23(B). PVK is a photoconductive polymer emitting in the blue.<sup>97</sup> The optical properties of ATTO-495 are pretty similar to those of MFG (Fig. 18(E)). Its absorption maximum in ethanol lies at  $20\,080\text{ cm}^{-1}$  and the emission maximum at  $19\,048\text{ cm}^{-1}$ . The spectral overlap regions between PVK and ATTO-495 and between ATTO-495 and  $\text{Ox}^+$  are large. ATTO-495 is thus expected to trap electronic excitation energy from PVK and pass it on to  $\text{Ox}^+$ .

Once ATTO-495 molecules are covalently bound on the zeolite external surface, the crystals can be handled easily. The ATTO-495,  $\text{Ox}^+$ -zeolite L crystals were embedded in PVK by preparing a polymer/dye-zeolite suspension in dichloromethane. Layers were prepared by evaporating the solvent. Fig. 23(D) shows the emission spectra of ATTO-495,  $\text{Ox}^+$ -zeolite L embedded in PVK sample (solid), and of ATTO-495,  $\text{Ox}^+$ -zeolite L sample (dashed) when the layers are excited at  $30\,300\text{ cm}^{-1}$ , where the absorption of the polymer is strong. In the sample without polymer, emissions of ATTO-495 and  $\text{Ox}^+$  are very weak; they are coming from the direct excitation of dyes, and both of them have very little absorptivity at  $30\,300\text{ cm}^{-1}$ . At the same time, bands of dyes in the sample with polymer are intense. This indicates that we can transfer electronic excitation energy from the photoconductive polymer PVK to the ATTO-495 stopcocks on the zeolite external surface, and even to the  $\text{Ox}^+$  molecules inside the zeolite channels. The excitation spectra of the layers recorded at  $16\,260\text{ cm}^{-1}$  where  $\text{Ox}^+$  emission is detected, Fig. 23(E), do support this conclusion. In the sample with PVK there is a typical band of the polymer around  $30\,000\text{ cm}^{-1}$ .

This is another indication that the polymer is able to generate  $\text{Ox}^+$  emission by energy transfer *via* intermediate ATTO-495 stopcock molecules.

### 6.5. Full and selective functionalization of the external crystal surface

In order to fully exploit the potential of dye-zeolite L materials, it is essential to control the interaction of an individual crystal with its environment. Therefore, appropriate functionalization of the external crystal surface is important, which is possible because base and coat of the crystals differ in their chemical reactivity.

Full coverage of the external crystal surface can *e.g.* be achieved by reacting the crystals with 3-aminopropyltriethoxysilane (APTS).<sup>98</sup> The result can be checked by first coupling the amino groups with a fluorescence marker and then examining the crystals under a fluorescence microscope. A fluorescence microscopy image of the APTS-modified crystals marked with fluorescein dye is reported in Fig. 24(A). It shows that the whole crystal surface is covered with the dye.

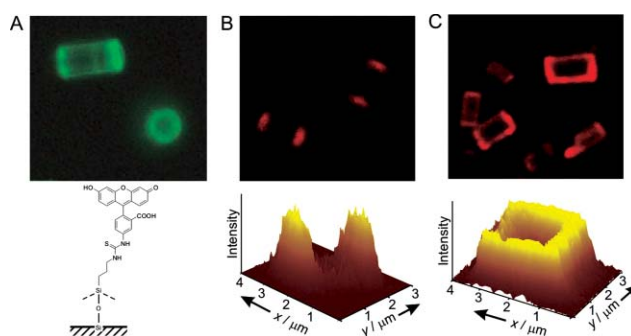
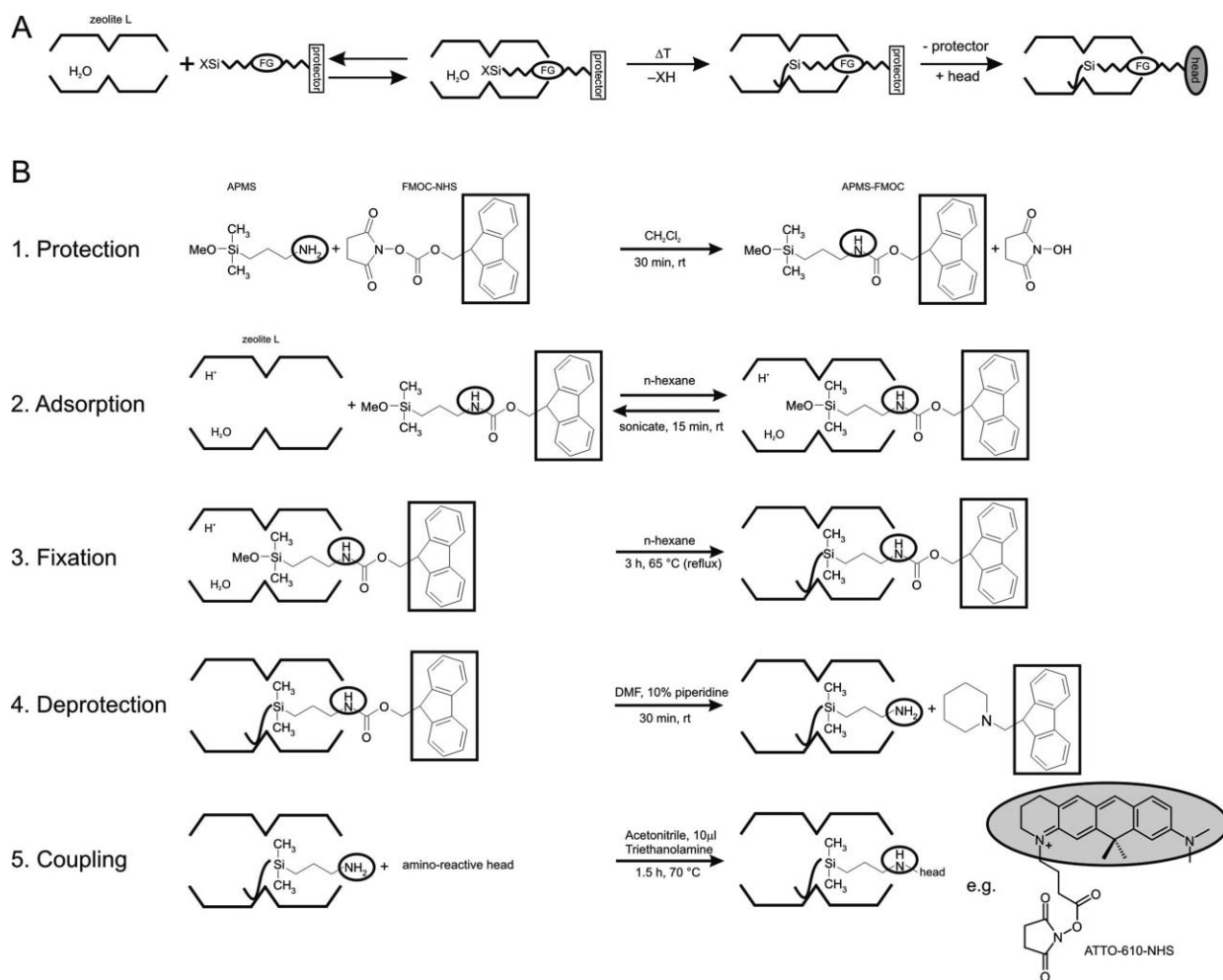


**Fig. 24** Fluorescence microscopy images of functionalized zeolite L crystals. (A) Fluorescence microscopy image of zeolite L with fluorescein covalently bound to the external surface. The length of the cylindrically shaped crystals is approximately  $5\text{ }\mu\text{m}$ . The crystal on the right is standing on its base.<sup>98</sup> (B) Functionalization of the base. Two APMS-functionalized and marked with ATTO-610-NHS crystals (top), and the corresponding relative intensity distribution of one of these crystals (bottom).<sup>88</sup> (C) Several base and coat functionalized crystals with APTES and marked with ATTO-610-NHS (top), and the corresponding relative intensity distribution of one of these crystals (bottom).<sup>88</sup>

It is often desirable to have a selective functionalization of the channel entrances. The principle of an elegant and general method for covalent attachment of stopcocks is shown in Scheme 6(A).<sup>88</sup> First, a stopcock molecule containing both functional ( $\text{NH}_2$ ,  $\text{SH}$  or  $\text{COOH}$ ) and protective groups is attached to the channel entrance. The protective group is then hydrolyzed, leaving behind a desired functional group that can react with an appropriate reactive reagent. Scheme 6(B) shows a five-step reaction scheme to obtain  $\text{NH}_2$ -functionalized zeolite L material using FMOc-protected (3-aminopropyl)methoxydimethylsilane (APMS-FMOc): (1) *Protection* of the functionalizing group with a molecule that is too big to enter the channels of zeolite L. This step is necessary to ensure that the stopcock enters the channels in the desired direction. (2) *Adsorption* of the reactive stopcock at the channel entrances of the zeolite crystals. (3) Reaction between the adsorbed stopcock and the channel interior, which leads to irreversible *fixation*. The nature of the bond is not well understood. We



**Scheme 6** Selective functionalization of the channel entrances. (A) Reaction principle of covalent functionalization of the channel entrances of zeolite L crystals. “FG”: desired group to functionalize the channel ends, “protector”: part of the molecule which is too big to enter the channel and which afterwards can be removed, “XSi”: group which can penetrate the channel and bind to the zeolite framework, “head”: the FG can be further reacted with a head if desired. (B) Reaction scheme to obtain  $\text{H}_2\text{N}$ -zeolite L precursor material selectively modified at the channel entrances to which any aminoreactive head-molecule can be reacted, e.g. ATTO-610-NHS.<sup>88</sup>

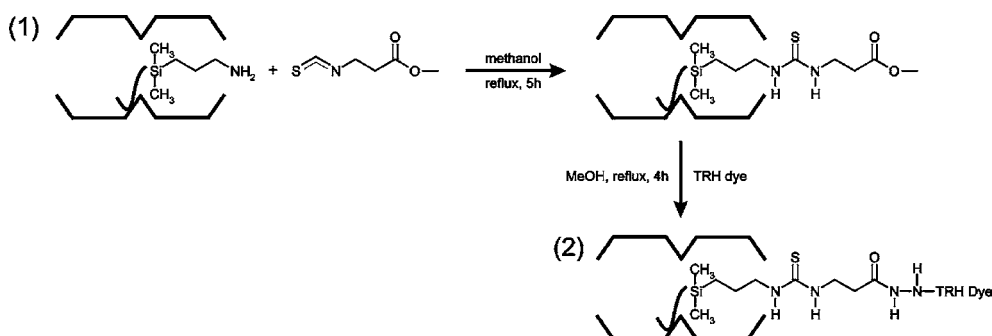
therefore symbolized by a hook. (4) *Removal of the protecting group*, leaving the crystals with free functionalizing groups at the channel entrances. (5) *Coupling of the head* bearing the desired property; it can be a fluorescing dye or another molecule.

It is important to adapt the amount of APMS-FMOC molecules to the number of channel entrances. The fluorescence microscopy image of the crystals prepared under this condition, after marking the  $\text{NH}_2$  groups with the red luminescent ATTO-610-NHS, is shown in Fig. 24(B). One can see red fluorescence of ATTO-610 only at the base of the crystal. The whole external crystal surface can be modified with  $\text{NH}_2$  groups if an excess of APMS-FMOC molecules with regard to number of channel entrances is used, as illustrated in Fig. 24(C). The shape of the stopcock used in step 1 influences the result of the procedure.

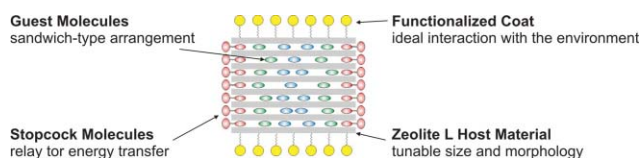
The possibility to use carboxyester functionalizations in addition to amino functionalizations widens the scope of chemicals that can be attached to the crystals, such as for example DNA.<sup>99</sup> The approach we have followed to synthesise such materials is

explained in Scheme 7. The idea develops in two phases, (1): preparing the amino-modified material by means of the procedure explained in Scheme 6; (2) reacting the free amino group attached to the end of each channel with the thiourea group from methyl-3-isothiocyanatopropionate.<sup>100</sup>

The different chemical properties of the base and the coat of zeolite L have been further explored by covalently linking different chromophores selectively to the base and the coat and by studying the photophysical properties of the individual crystals of the so obtained samples.<sup>101</sup> The now available possibilities to build complex functionalities with dye-loaded zeolite L crystals are remarkable. Scheme 8 illustrates that first the desired structure inside of the crystals is build, followed by modifying the channel entrances in the desired way and finally functionalizing the coat. The individual functionalizations must not necessarily be made with fluorescent dyes. Some steps may also be directed towards appropriate sealing of the channels, influencing the solubilization properties, changing the reactivity, and other targets.



**Scheme 7** Reaction principle for transforming an amino group into a carboxyester group at the channel entrance: (1) The amino groups located at the channel entrances are reacted with methyl-3-isothiocyanatopropionate. (2) The terminal carboxyester groups are then coupled with a correspondingly reactive dye; THR was used as an example.<sup>86</sup>



## 6.6. Orientation of the electronic transition dipole moments (ETDM)

The energy transfer rate constant depends on the relative orientation of the ETDM of donor and acceptor described by the orientation factor  $\kappa^2_{D^*A}$ , see Scheme 1 and eqn (3).  $\kappa^2_{D^*A}$  takes values from 0 when the ETDM are perpendicular with respect to each other, Fig. 25(A), up to 4 when they are collinear, and it is one when the ETDM are parallel. It is therefore important to control the relative orientation of the ETDM of a stopcock and a guest molecule inside the channel. We show in Fig. 25 possible orientations of ETDM of stopcocks and a typical cone type distribution of the ETDM of guest molecules inside the channels. Energy transfer between the stopcocks and the molecules inside can be maximized or minimized depending on their relative orientations. It is usually easy to realize a large  $\kappa^2_{D^*A}$  value for a parallel orientation of the stopcock transition moment (Fig. 25(D)) or even for parallel and perpendicular orientation (Fig. 25(E)). The least critical is the case of spherical orientation shown in Fig. 25(F). All cases (A) to (F) can be realized, and we

have an example of stopcock molecule for each situation shown. There is plenty of room, however, for synthetic chemists to do much better than what is currently available.

## 7. Organization and communication

Hierarchically organized structures, presenting successive ordering from the molecular up to macroscopic scale are subject of great interest due to the relationship between the molecular arrangements and the macroscopic properties.<sup>102-104</sup> This is an aspect that makes nanotechnologies appealing in nano/micro electronics, in photonics and in biology. Organisation of quantum-sized particles, of nanotubes, and of microporous materials have been studied on different surfaces and used for purposes in science, technology, diagnostics and medicine.<sup>105-114</sup> Size, shape and surface composition of the objects but also the properties of the surface on which they should be organized play a decisive role and in some cases determine not only the quality of the self-assembly but also its macroscopic properties. Base and coat of zeolite L have different chemical properties, and dyes inside the channels are well oriented and can be organized into distinctive patterns. Zeolite L crystals containing oriented fluorophores in their parallel nanochannels possess efficient fluorescent properties, that make them ideal host-guest structures for the exploitation of energy transfer and energy funneling processes in the fields of optoelectronics and photonics, provided that they can be properly organized.

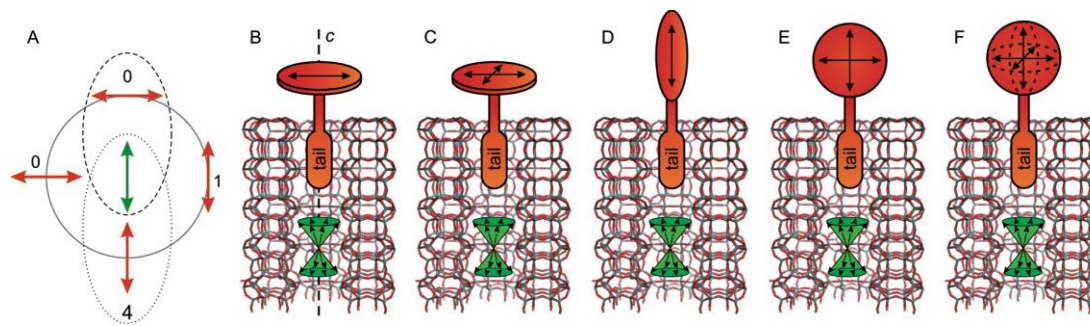


**Fig. 25** Orientation of the ETDM. (A) Selected values of orientation factor  $\kappa^2$  (values) of the donor-acceptor pairs for  $\phi = 0^\circ$ . Donor is presented as green arrow, acceptor as red arrow. (B)-(F): examples of orientation of the transition dipole moment of stopcock molecule (in orange); (B) perpendicular to the channel axis ( $c$ -axis), (C) in plane, (D) parallel to the channel axis, (E) parallel and perpendicular orientations, (F) spherical orientations. In green the typical cone type distribution of the transition moments of guest molecules inside the channels is shown.

Self-assembly strategies in the organization of matter make hierarchical ordering attractive by avoiding expensive techniques such as photolithography. Assembling zeolite crystals into well-defined macroscopic structures is of particular interest, considering that zeolites are ideal host materials for supramolecular organization. The generation of zeolite patterns adds a further level of organization, thus extending the ordering from the molecular to the macroscopic scale. Large zeolite crystals can be aligned by an electric field<sup>115</sup> or by mechanically shaking them into the grooves of a micro-structured surface.<sup>116</sup> However, single crystals in this size regime are not accessible for most zeolite types, and are furthermore not practical for most purposes. For smaller crystals, a distinct interaction between the crystals and specific parts of the substrate is necessary to achieve ordering into defined patterns. It has been shown that zeolite L crystals containing a large variety of different molecules can be arranged in nearly any desired manner by means of self-organization methods, as will be explained in the next section, after which communication will be addressed.

### 7.1. Organizing the crystals

We first explain a simple method for aligning zeolite L crystals of an aspect ratio length to diameter significantly larger than one by a method that has been successful for elongated molecules dissolved in a polymer for a long time and can be regarded as a classical experiment.<sup>117</sup> The concept is to align the crystals in a liquid by circulating the zeolite suspension in a tube. The flow rate of a liquid in a tube is different at every point of the cross section. The velocity distribution resembles a parabola due to friction at the tube walls. Due to the different force effects, the elongated crystals align parallel to the tube walls. About 6 000 nm long crystals with an aspect ratio length to diameter of 2.5 were used for the experiment shown in Fig. 26. Half of the amount was loaded with Ox<sup>+</sup> and the other half with MC<sup>+</sup>. The blue fluorescent MC<sup>+</sup> is aligned parallel to the zeolite channels, while the red fluorescent Ox<sup>+</sup> is smaller and oriented at about 72°. The same amount of each sample was suspended in water and the suspension was pumped through a flexible tube. Between two flexible plastic tubes a quartz glass part was inserted thus enabling microscopic analyses of the

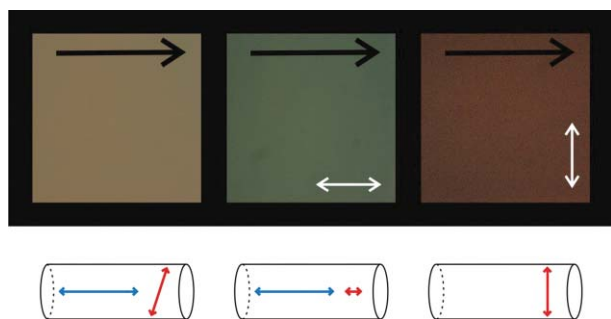


**Fig. 26** Fluorescence microscopy images of a suspension flowing through a tube at a flow rate of 2 mL min<sup>-1</sup>, containing a 1:1 mixture of Ox<sup>+</sup>-zeolite L and MC<sup>+</sup>-zeolite L. The flow direction is indicated by the black arrows. Left: not polarised. Middle and right: polarised. The white double arrows indicate the orientation of the transmitted light. Bottom: schematic representation of the crystals, blue and red arrows represent the ETDM of MC<sup>+</sup> and Ox<sup>+</sup>, respectively, and their projections to the transmission axis of the polarizer (middle and right).<sup>118</sup>

suspension flowing through the system. The zeolite suspension was excited at 400 nm to 440 nm and the emission detected through a 475 nm cut-off filter. The images in Fig. 26 show a section of the quartz plates under the microscope. The intense colour change of the not polarised and the polarised microscope images illustrate the considerable anisotropy of the samples. As the zeolite suspension has a thickness of 1 mm and the crystals are in motion, single particles are not resolved.<sup>118</sup> Similar observations were made by embedding crystals loaded with Py<sup>+</sup> into a PVC polymer film which was then stretched by a factor of 3 to 5, as illustrated in Fig. 27(A, right).<sup>42</sup>

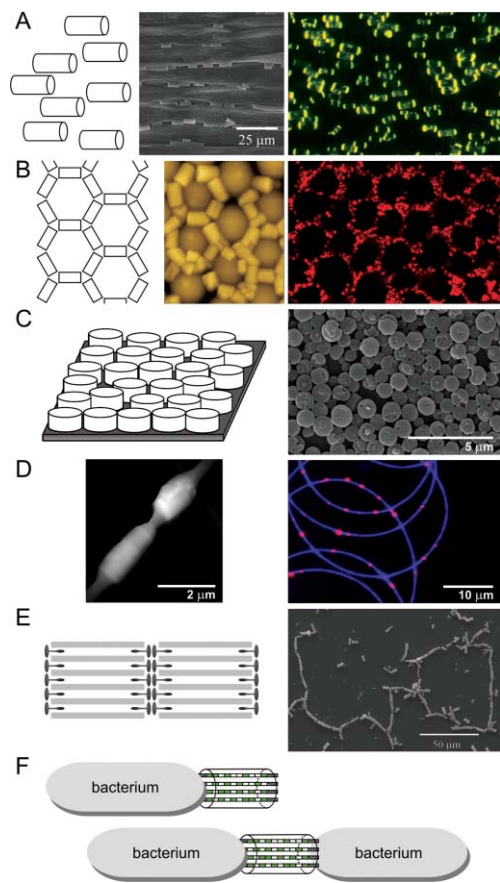


**Fig. 27** Organizations of zeolite L crystals. (A) Nematic phase. Middle: SEM image of zeolite L crystals aligned on the top side of a rough hawk's beard's (*crepis biennis*) petal.<sup>118</sup> Right: fluorescence microscopy image of Py<sup>+</sup>-zeolite L crystals aligned in a stretched PVC plastic film. The Py<sup>+</sup> molecules are located at the channel ends due to the short insertion time that was used when preparing the material.<sup>42</sup> (B) Hexagonal arrangement. Middle: dye-zeolite L crystals organized by a surface-tension-driven auto-assembly process on a PDMS/PS film.<sup>120</sup> Right: fluorescence microscope image of Ox<sup>+</sup>-zeolites aligned on the petal of a horned pansy (*viola cornuta*).<sup>118</sup> (C) Monolayers of standing zeolite L crystals. Left: SEM image of a monolayer.<sup>121,122</sup> (D) Nanofiber. Left: AFM image of nanofiber with embedded zeolite L crystals. The crystals are oriented along the fiber axis. Right: fluorescence image PEO/DDT nanofiber (blue) with embedded Ox<sup>+</sup>-zeolite crystals (red sparks).<sup>123</sup> (E) Chains. Right: SEM image of zeolite crystals linked together by modifying the channel entrances with the cationic dye D291.<sup>42</sup> (F) A 1:1 assembly of zeolite L/bacterium in PBS buffer solution and self-assembly of two bacteria with functionalized 1 μm zeolite L as the junction.<sup>124</sup>

An interesting phenomenon was observed when the petals of different flowers were immersed into a suspension containing  $\text{Ox}^+$ -zeolite L crystals: The zeolites align into patterns which are distinct for each flower species. On the petal of a straw flower (*helichrysum bracteatum*) they align into parallel lanes, as can be seen on the SEM image shown in Fig. 27(A, middle). The straw flower exhibits elongated epidermis cells. The alignment of the  $\text{Ox}^+$ -loaded zeolites on the straw flower petal can also be observed under a fluorescence microscope. Polarised microscopy images show that most zeolites are oriented in the same direction. On the petal of a horned pansy (*viola cornuta*), they align into hexagons, Fig. 27(B, right). This alignment is not determined by topological forces. In places which exhibit self-cleaning properties, zeolites are not adsorbed.<sup>118</sup>

Strategies implying self assembly by minimization of interfacial free energy have been applied to position small objects at the micrometric scale.<sup>119</sup> A novel approach towards micro-patterning employing a surface tension pattern was realized by Yunus *et al.*<sup>120</sup> It was shown that zeolite L crystals containing dyes in their parallel nanochannels can be well organized in a hexagonal arrangement on polydimethylsiloxane (PDMS) films obtained through molding of self-assembled ordered macroporous polystyrene (PS) films. We show in Fig. 27(B, middle) a SEM image of such a material. It demonstrates that surface tension interactions can be considered as a powerful tool for manipulation at the micrometric scale, since, based on self-assembling processes, we are able to hierarchically organize molecular dyes at a macroscopic level.

Another possibility of achieving a higher level of organization is the controlled assembly of the zeolite crystals into oriented structures where the cylindrically shaped zeolite L are standing on their base. This has as a consequence the alignment of a large number of one-dimensional channels as explained in Fig. 27(C, left). An underlying principle that has to be respected when preparing such a material is that the interaction between the base of the zeolite L crystals and the substrate must be stronger or much stronger than with the coat and, importantly, any interaction among the zeolite crystals. Working with an excess of crystals, fixing them in the right way to the substrate and washing away the excess material has under these conditions a high chance to lead to the desired material. Subsequent insertion of dye molecules into the channels and addition of stopcocks is only possible if the channels are not blocked or damaged during the preparation of the monolayer. Preparing such layers is possible in a variety of ways, an example is illustrated in Fig. 27(C, right).<sup>42,114,121,122,125</sup> Modifying the zeolites by inserting dyes and attaching stopcocks leads to materials with exciting properties,<sup>44,80,95,126</sup> *e.g.* to systems where electronic excitation energy is transported in one direction only,<sup>121</sup> as will be discussed in Section 8. Embedding zeolite L crystals, 600–800 nm in diameter and 1  $\mu\text{m}$  in length, into nanometric polymer fibers of a wire diameter down to 150 nm was shown to be possible by means of an electrospinning technique. The zeolite crystals are well oriented in the polymer wires with their crystal axis parallel to the fiber axis. Dye-loaded zeolites, integrated into nanowires, form very bright nanometric light sources emitting polarized light at visible wavelengths, as illustrated in Fig. 27(D).<sup>123</sup> This new materials is currently exploited in advanced nanophotonic applications. Electrospinning is a simple and efficient process for the fabrication of long fibers with diameters ranging from the micro and nanoscale.<sup>127,128</sup> - Creating one-dimensional zeolite

assemblies is challenging and may lead to micro-barcode used for bio-imaging and tagging purposes.<sup>129</sup> A very elegant way to create one-dimensional arrays of zeolite L crystals is to hold them together through multiple coordinative interactions. The reversible nature of the coordinative bond allows the arrays to maximize the base to base interaction between crystals.<sup>79</sup> We show in Fig. 27(E) zeolite L crystals that assemble into rods due to van der Waals interactions, after modifying the channel entrances with the D291, Table 4.<sup>42</sup> Recently functionalized biocompatible artificial nanocontainers (among functionalized zeolite L according to<sup>88</sup> containing  $\text{Py}^+$ ) have been successfully attached to nonpathogenic bacteria (*Escherichia coli*; *E. coli*). It was demonstrated that the living species attached to the zeolite can be easily visualized by using fluorescence spectroscopy, owing to the particularly defined geometrical arrangement of the zeolite and bacteria. It has been shown that two bacteria self-organize by using the nanocontainer as a junction owing to the particularly defined geometrical arrangement of the zeolite and bacteria.<sup>124</sup> This means that self-assembly of functional materials and living systems is possible through a chemically programmed construction. It will be fascinating to explore the consequences of this.

These results demonstrate that surface tension, van der Waals, electrostatic and coordinative interactions are powerful tools for manipulation at the nano- and micrometric scale, allowing to hierarchically organize molecular dyes at a macroscopic level based on self-assembling processes.

## 7.2. Communication *via* stopcock

The stopcock principle allows communication between dyes inside the channels and a reaction centre outside of the crystal *via* energy transfer. This is schematically explained in Fig. 28. The reaction centre can be a molecule, a polymer matrix, a semiconductor, a quantum sized particle, a molecular- or nano-magnet, and a biochemical or biological object. From the results reported in Sections 6 and 7 different kind of communication can be deduced.

Here we discuss the possibility of communication with a biochemical object. The stopcock-plugged dye-zeolite L materials can be used as luminescent labels for analytical purposes. The reaction principle is shown in Fig. 29(A). Biotin (biotin-X) has been attached to dye1-zeolite L crystals by the method of sequential functionalization described in Section 6.5. DMPOPOP has been used as dye1 and the zeolite L nanodiscs (2) in Fig. 3 as host. The excitation and the fluorescence spectra of the samples are shown in Fig. 29(B). To the biotin-plugged dye1-zeolite L material a weak binding antigen modified with ATTO-488 (dye2) (anti-biotin-IgG-ATTO-488) was added, and the result was studied by measuring the fluorescence spectra in a buffer of pH 7, Fig. 29(B). The emission upon excitation at 340 nm and the excitation spectra, recorded at 600 nm, of pure biotin-plugged dye1-zeolite L (spectra in grey) identify only one band, that of dye1. Reaction with antigen-dye2 (spectra in black) leads to an additional band, that of dye2, in the excitation spectrum. The emission spectrum, also upon excitation at 340 nm (specific excitation of dye1), shows that the dye1 emission is considerably quenched, while the dye2 emission comes up intensely—due to Förster energy transfer, as the distance between the dye1 guest and the dye2 reaction centre molecules is sufficiently short. This example shows that functional

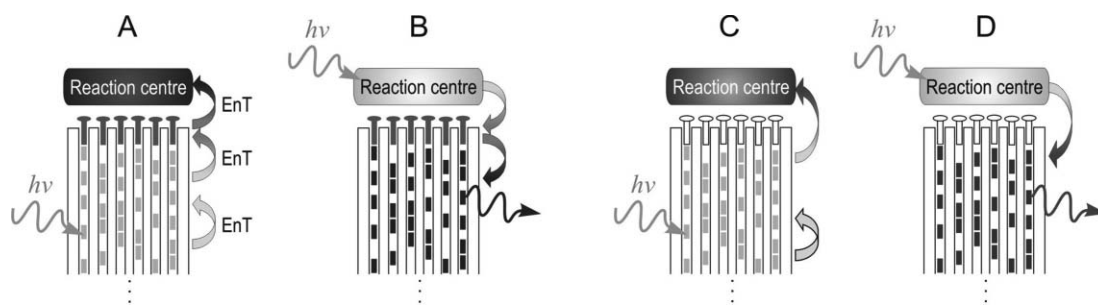


**Fig. 28** Communication of guest molecules with an external reaction centre *via* energy transfer. Stopcock molecules can be luminescent and hence participate in energy transfer from guest molecules to the reaction centre, (A) and (B), or they can be non-luminescent, just linkers to the environment, cases (C) and (D). EnT can be directed from the guest molecules to the RC, (A) and (C), or in the opposite direction, (B) and (D).

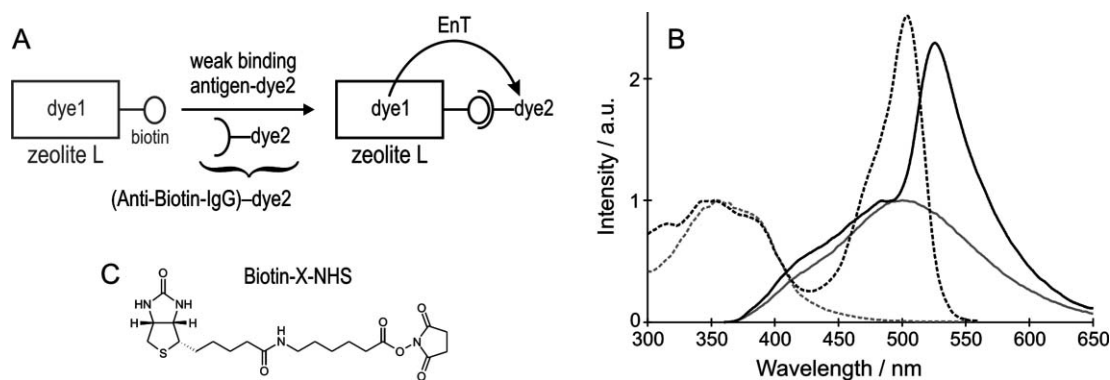


**Fig. 29** Functional energy transfer bio-label. (A) Reaction principle. (B) Excitation (emission at 600 nm, dashed line) and emission (excitation at 340 nm, solid line) spectra before reaction (grey lines) and after reaction (black lines) of biotin-plugged dye1–zeolite L with antigen-dye2, measured in a pH 7 buffer. Spectra are scaled to the peak height of dye1 absorption/emission, respectively. (C) Structure of Biotin-X-NHS.

energy transfer bio-labels based on dye–zeolite L systems are feasible.

## 8. Energy transfer in oriented dye1,dye2–zeolite L monolayers

In device chemistry, a high degree of supramolecular organisation is usually required for achieving desired macroscopic properties. The possibility to arrange zeolite L crystals in densely packed, oriented monolayers gives access to such higher level of structural organisation. It expands our options for the creation of photonic devices. Supramolecular organization of dyes inside the one-dimensional channel system has been realised, quasi-one dimensional energy transfer has been observed, and it has been demonstrated that the dye-loaded zeolite materials can be interfaced with the environment (be it a polymer, a semiconductor or a biochemical object) *via* stopcock molecules. The new hierarchy of structural order attained by organising supramolecular functional dye–zeolite crystals into oriented monolayers can be extended by sequentially filling the zeolite channels with different dyes. This is shown schematically in Fig. 30(top). Fig. 30(bottom) presents fluorescence microscopy images proving that the desired material has been obtained. We prepared a DTCl, MeAc<sup>+</sup>–zeolite L monolayer, by first inserting MeAc<sup>+</sup> (green dye) followed by DTCl (red dye) into the zeolite channels of an already prepared monolayer. Some crystals were then broken off from the monolayer for the optical microscopy investigation by scratching

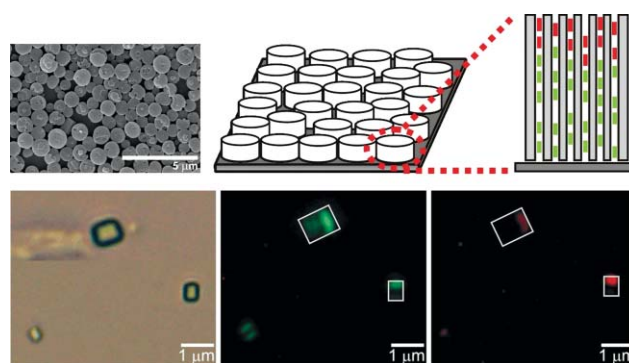


**Fig. 30** Dye–zeolite L monolayer on glass. Top: SEM image and of a zeolite L monolayer, showing that the crystals are oriented with the channel axis perpendicular to the substrate. A schematic representation of the same is shown in the middle and a scheme of a crystal sequentially loaded with green and red dyes on the right. Bottom: fluorescence microscopy images of DTCl,MeAc<sup>+</sup>–zeolite L crystals removed from a zeolite L monolayer. Left: Under white light. Middle: specific excitation of MeAc<sup>+</sup> at 470–490 nm. Right: specific excitation of DTCl at 545–580 nm.<sup>44,80</sup>

the layers with a spatula. Fluorescence can only be detected at one end of the crystals. This was true for a representative amount of the zeolite L crystals. This observation proves that after calcination of a zeolite L monolayer, dyes can enter the channels only from one side. It forms the basis for systems where excitation energy is transported in one direction as we will show below.

In another experiment, an oriented monolayer was prepared from Ox1–zeolite L crystals. It was then modified with Ru-ph4-TMS stopcocks. This donor–acceptor pair was chosen because of the efficient energy transfer that was recently observed between them, see Fig. 19 and Fig. 21.<sup>83</sup> The aim of the experiment was to see, whether a unidirectional energy transfer from the stopcock to the Ox1 could be realised in a monolayer system. Results obtained in such an experiment are shown in Fig. 31. The emission spectrum resulting from selective excitation of the Ru<sup>2+</sup> complex at 450 nm is

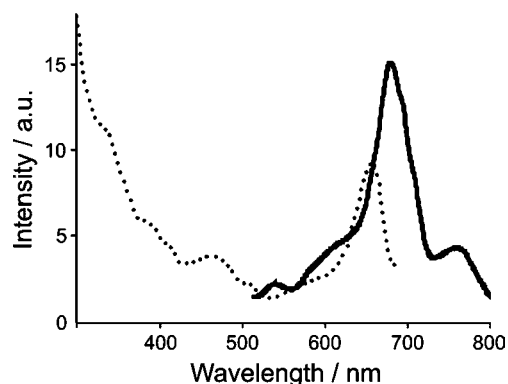


**Fig. 31** Energy transfer in an oriented Ru-ph4-TMS, Ox1–zeolite L monolayer. Excitation (dotted line) and emission (solid line) spectra of an oriented Ru-ph4-TMS, Ox1–zeolite L monolayer. The emission spectrum was observed after excitation at 450 nm, where Ru-ph4-TMS is selectively excited. The excitation spectrum was recorded at 710 nm.<sup>80</sup>

shown as a solid line. The excitation spectrum, shown as a dashed line, was detected at the emission maximum of Ox1<sup>+</sup> (710 nm). The luminescence spectra show very nicely that energy transfer from Ru-ph4-TMS to Ox1<sup>+</sup> takes place also in this type of system.

We report in Fig. 32 energy transfer in oriented dye1,dye2–zeolite L monolayers that illustrate that any combination of unidirectional energy transfer systems can be realised, namely between dyes organized inside of the channels (left), between a donor stopcock to acceptors inside (middle), similar as reported in Fig. 30, and from donor molecules inside to an acceptor stopcock (right). These systems can be considered as the first unidirectional antenna system realized on a macroscopic scale.<sup>121,122</sup>

An antenna material which absorbs all light in the right wavelength range and transfers it by radiationless energy transfer to a device like a semiconductor offers a unique possibility for developing dye sensitized solar cells or luminescent solar concentrators. This kind of sensitised solar cell functions by first absorbing light over a broad spectral range in the zeolite antenna material. The excitation energy migrates radiationlessly among the inserted dyes towards the stopcock molecules. From there, Förster energy transfer to the semiconductor takes place across a thin insulating layer. The injected energy can now be used for driving the charge separation process in the active medium. Finally, the resulting electrical current is collected *via* appropriate contacts. We show in Fig. 33 two strategies that can be followed, the one on the left applicable for thin layer silicon cells and the right for organic solar cells where the design must match the short free path lengths of the charge carriers in such devices.<sup>27,80,89,130</sup> Phthalocyanine

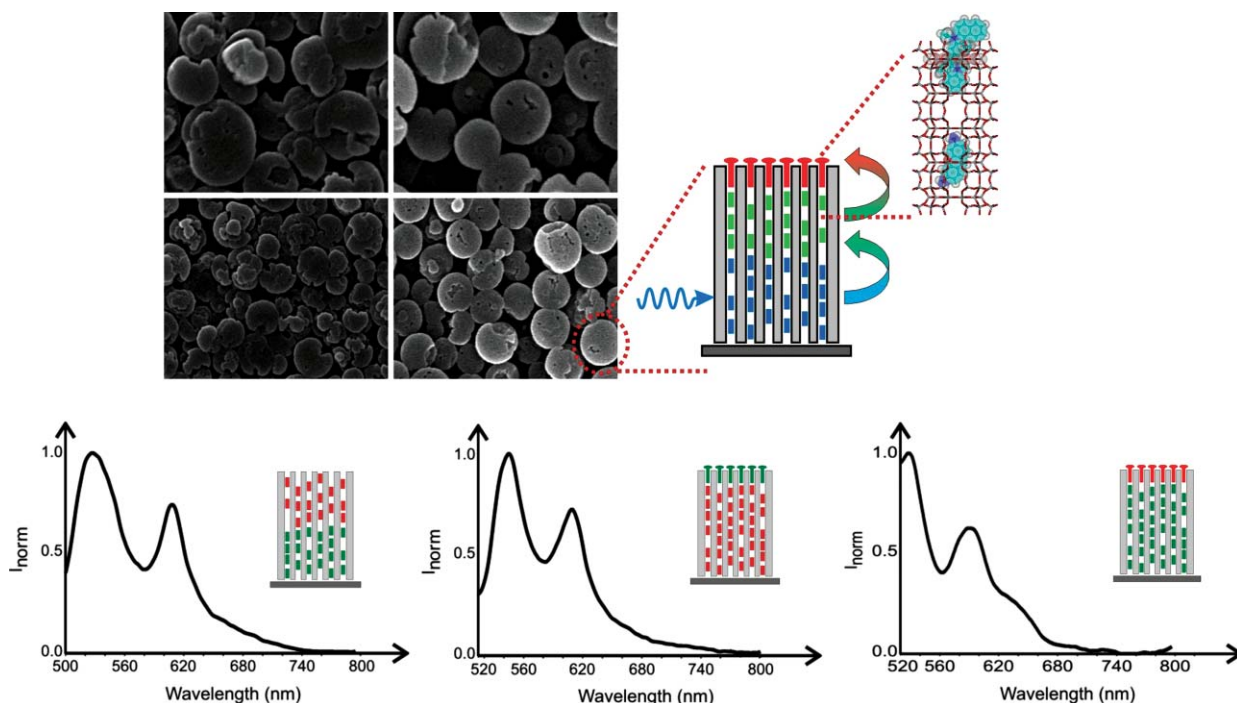


**Fig. 32** Energy transfer in oriented dye1,dye2–zeolite L monolayers. Top: the picture shows SEM images of two different layers at two different magnifications, a scheme of a zeolite crystal containing 2 dyes and modified with a stopcock, and a magnification of one channel. Bottom: emission of donor and acceptor loaded zeolite L crystals arranged as oriented monolayers on a glass plate. The spectra of the three samples have been scaled to the same height at the maxima. (A) Ox<sup>+</sup>,Py<sup>+</sup>–zeolite L monolayer. The emission spectrum was recorded after selective excitation of Py<sup>+</sup> at 460 nm. (B) ATTO-520,Ox<sup>+</sup>–zeolite L monolayer. The emission spectrum was recorded after selective excitation of ATTO-520 at 460 nm. (C) Cy02702,Py<sup>+</sup>–zeolite L monolayer. The emission spectrum was recorded after selective excitation of Py<sup>+</sup> at 460 nm.<sup>121</sup>

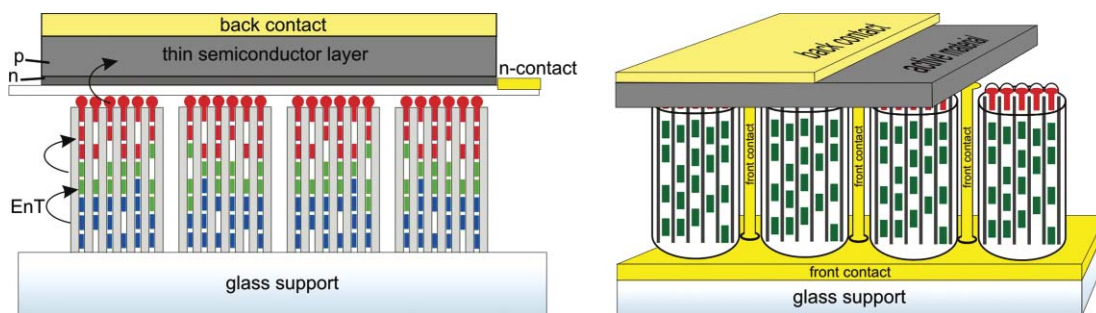


**Fig. 33** Principle of dye sensitized solar cells. Arranging crystals with their *c*-axes perpendicular to the surface of a semiconductor and a length of 50 nm up to a few hundred nm range allows transport of the excitation energy towards the zeolite-semiconductor interface by energy migration. Stopcock molecules are placed only at one channel end to allow energy transfer. The semiconductor layer can be very thin, because the electron-hole pairs form near the surface. The transfer of electrons from antenna to semiconductor is prevented by introducing a thin insulating layer, preferably directly into the stopcock. The scheme on the left shows a principle related *e.g.* to thin layer silicon devices. The scheme on the right is related to organic solar or plastic solar cells. The white area on top of the head is an insulating part directly integrated into the stopcock. The zeolite materials is enlarged with respect to the rest of the device.

stopcock molecules where the insulating layer between the head and the stopcock, needed to prevent electron transfer, is directly integrated into the molecule are especially attractive.<sup>77</sup> Energy can also be transferred from an appropriately chosen semiconductor to the antenna composites by reversing the current and putting a voltage over the semiconductor. The dye-zeolite composites on the semiconductor surface subsequently lose their energy by emitting light. The colour of the emission can be tuned by adapting the ratio of blue, yellow, and red fluorescent dyes, which means that white light emission is possible. High energy efficiency and easily adaptable emission spectra are expected for (O)LEDs made by using this principle.<sup>27</sup>

## 9. Spectroscopy on dye-loaded zeolite L monolayers

Dye-loaded zeolite L monolayers are interesting not only because of practical applications, but also for advanced study of photo-physical and photochemical properties of dyes enclosed in the one-dimensional zeolite channels, since good quality absorption spectra of monolayers can be measured. Excitation spectra reveal only those transitions and processes which appear in emission, while the absorption spectrum reveals all of them. Some quenching species, *e.g.* doubly-protonated oxonine,<sup>80</sup> are non-fluorescent and hence can be seen only in the absorption spectrum. The absorption spectra on monolayers will also help to better study the question of J-aggregation coupling of dyes inside the channels described in Section 3.4.

Prior to measure the absorption spectrum of a monolayer, the light scattering of zeolite L has to be suppressed.<sup>131</sup> As one can see from the photographic image of a monolayer in Fig. 34(left), zeolite L possesses considerable light scattering in the visible range even being arranged as monolayer. One can overcome this problem *via* refractive index matching, when a monolayer is covered with a polymer of similar to zeolite refractive index. Fig. 34(right) shows similar monolayer coated with a polymer; the monolayer is nicely transparent.<sup>132</sup>

Dye-loaded zeolite L crystals are optically anisotropic. This comes from the double-cone distribution of the ETDM within a crystal as discussed in Section 3.3. As in a monolayer all crystals are parallel to each other, the optical anisotropy of the individual



**Fig. 34** Photographic images of unloaded zeolite L monolayers on a glass substrate. Left: uncoated monolayer. Right: similar sample coated with Columbia Resin 39 (CR39).

crystal becomes a macroscopic property which can be observed by measuring the absorption spectra at different angles of incident light.

### 9.1. Optical anisotropy of dye-loaded zeolite L monolayers observed in the absorption spectra

The measurement situation of the experiment is shown in Fig. 35. Incident light is linearly polarized; its electric component is perpendicular to the direction of propagation. The incident angle of light  $\alpha$  is the angle between the horizontally polarized light and the monolayer support. The orientation of the ETDM of a molecule inside the channel is defined by the angle  $\beta$ .

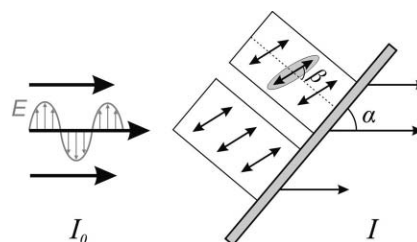


**Fig. 35** Schematic representation of the measurement situation.  $\alpha$  is the angle between the horizontally polarized light and the monolayer support, and  $\beta$  is the angle between the ETDM of the molecule and the channel axis.  $I_0$  is the incoming light and  $I$  is the transmitted light.

Depending on the value  $\beta$  there are three typical situations, Fig. 36: (A) Molecules oriented perpendicular to the channel axis,  $\beta = 90^\circ$ . If light falls parallel to the monolayer support ( $\alpha = 0^\circ$ ), no

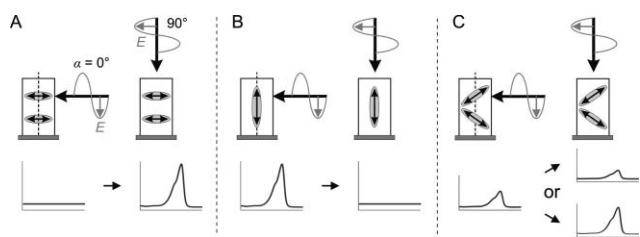


**Fig. 36** Dependence of the monolayer absorbance on the orientation of molecules inside the channel (angle  $\beta$ ), and on the incident angle of light (angle  $a$ ).

absorption will take place, since the ETDM are perpendicular to the electric vector of the incident light and, hence, the molecules can not be excited. However, if light falls perpendicular to the support ( $a = 90^\circ$ ), electric vector and ETDM are parallel, which means maximal absorbance; (B) Molecules oriented along to the channel axis,  $\beta = 0^\circ$ . Light falling parallel to the support is a favourable situation for absorption, and no absorption happens if light falls perpendicular; (C) Molecules oriented at an angle different from  $0^\circ$  and  $90^\circ$ ,  $0^\circ < \beta < 90^\circ$ . If light falls parallel to the monolayer support, some absorption will take place; if light falls perpendicular, absorption will increase or decrease depending on the value of angle  $\beta$ .

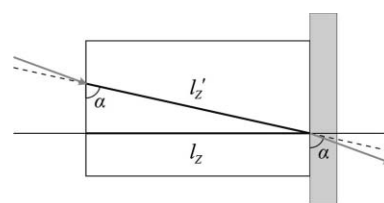
The dependence function of absorbance is easy to find for the 2D case. The following expression holds:<sup>63</sup>

$$f(a, \beta) = |\cos(a + \beta)| + |\cos(a - \beta)| \quad (12)$$

The experimentally available counterpart to  $f(a, \beta)$  is e.g. the maximum of the absorption spectrum  $A_{\max}$  at the corresponding angles. The lengthening of the beam path at the angles  $a$  different from  $90^\circ$ , which leads to the increase of absorbance, should be taken into account when comparing absorption spectra at different incident angles. Correction to the same path length is given by:

$$l_z = l'_z \sin a \quad (13)$$

where  $l_z$  is the width of a monolayer which corresponds to the length of the zeolite crystals, and  $l'_z$  is the path length of the beam; see Scheme 9. The deviations of  $a$  due to light refraction at the



**Scheme 9** Lengthening of the beam path at incident angles  $a$  different from  $90^\circ$ .

interfaces air–zeolite, zeolite–support, support–air are not taken into account. Hence, to set the absorption spectrum to the path length  $l_z$ , the spectrum  $A_a(\lambda)$  measured at a given  $a$  should be multiplied by the sine of this angle:

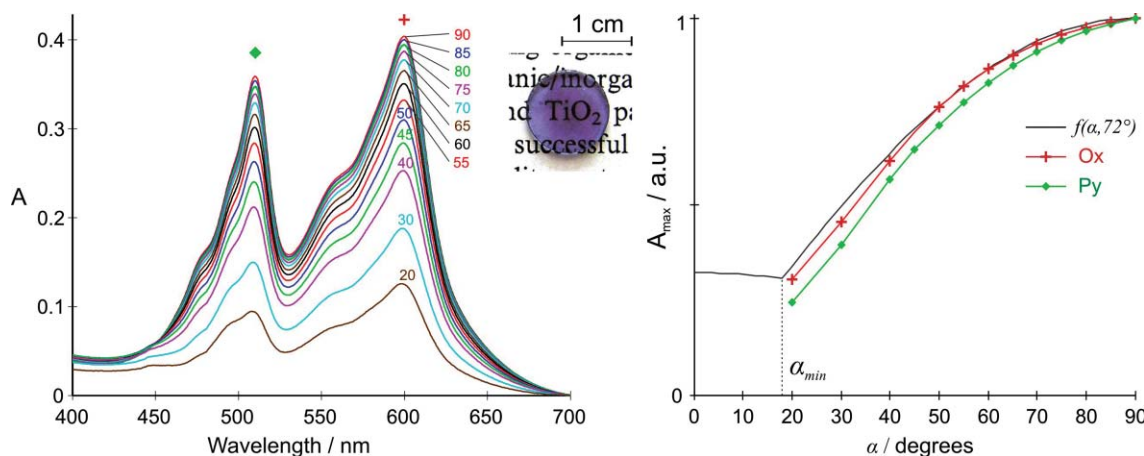
$$A_{\text{corr}}(\lambda) = A_a(\lambda) \sin a \quad (14)$$

Fig. 37(left) shows absorption spectra of a  $\text{Py}^+, \text{Ox}^+$ -zeolite L monolayer measured at different incident angles and corrected to the same path length. The ETDM of both dyes are oriented at  $72^\circ$  with respect to the channel axis. Absorbance of both bands decreases with decreasing  $a$ , which shows that the monolayer is optically anisotropic. The scaled values of the absorbance maxima, at 520 nm for  $\text{Py}^+$  and at 600 nm for  $\text{Ox}^+$ , were compared with the theoretical function  $f(a, 72^\circ)$ . Fig. 37(right) shows that the optical anisotropy of the sample nicely follows eqn (12) for both dyes.

Another example is a DXP-loaded zeolite L monolayer, Fig. 38. The ETDM of DXP was found to be oriented along the channel axis,  $\beta \approx 0^\circ$ . The optical anisotropy is demonstrated also for this monolayer. The absorptivity at  $a = 90^\circ$  is larger than expected. We do not understand this and think that more precise measurements would be needed.

The orientation angle  $\beta$  can be found from the dependence function  $f(a, \beta)$ . If  $a_{\min}$  is the angle where the function has a minimal value, as shown in Fig. 37(right),  $\beta$  can be found from the following simple expression:

$$\beta = 90^\circ - a_{\min} \quad (15)$$



**Fig. 37**  $\text{Py}^+, \text{Ox}^+$ -loaded zeolite L monolayer covered with poly(vinyl alcohol). Left: absorption spectra measured at different incident angles  $a$  and corrected to the same path length. The numbers correspond to the value of  $a$ . Middle: photographic image of the sample. Right: comparison of scaled absorbance maxima  $A_{\max}$  with the theoretical function  $f(a, 72^\circ)$ . Points have been connected by a line for better visualisation.

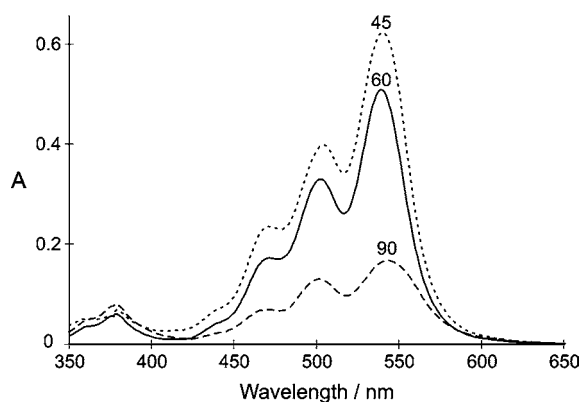


**Fig. 38** Absorption spectra of DXP-loaded zeolite L monolayer, immersed in toluene to suppress the light-scattering, measured at different incident angles  $\alpha$  and scaled to the same path length. The numbers correspond to the values of  $\alpha$ .

One can, in principle, use this procedure of measuring the absorption spectra at different angles  $\alpha$  as a method to determine the orientation angle  $\beta$  of the ETDM of the dye molecule.

## 9.2. Extinction coefficient in oriented dye-loaded zeolite L crystals

The double-cone distribution of the ETDM causes not only optical anisotropy of a dye-loaded monolayer but also a different extinction coefficients of the dye compared to solution. The unpolarized incident light is directed along the  $z$ -axis and consist of photons with electric vectors of all possible orientations in the  $x,y$ -plane. The whole variety of orientations is reduced to only two, coinciding with the  $x$ - and  $y$ -axis,  $E_x$  and  $E_y$ , respectively, to

simplify the discussion, Fig. 39. This representation is correct as long as the distribution of orientations is homogeneous.

We consider the situation in solution, where the molecules are randomly oriented, as represented by three ETDM oriented along the axes in Fig. 39. Photon  $E_x$  can hit only one of three possible orientations of molecules, the one with a ETDM oriented along the  $x$ -axis. Hence, the probability for a photon  $E_x$  to excite a molecule is  $1/3$ . The same is true for a photon  $E_y$ ; the probability is  $1/3$  since a photon can excite only the molecules with the ETDM oriented along the  $y$ -axis. Thus the mean probability to excite a molecule is  $1/3$ .

Let us compare this situation with the dye-loaded monolayer. In a monolayer, the orientation of all molecules is fixed with regard to the  $z$ -axis but the ETDM can have any orientation in the  $x,y$ -plane, which is represented by their projections to this plane. Hence, the probability for a photon to excite a molecule is higher compared to solution; it is equal to  $1/2$  for both  $E_x$  and  $E_y$  resulting in a mean probability of  $1/2$ . Since the extinction coefficient of a dye is directly proportional to the mean probability, the extinction coefficient in a monolayer is  $3/2$  times higher than in solution, but only for the projection of the transition dipole moment on the  $x,y$ -plane. Taking into account the length of the projection:

$$\frac{\mu_{xy}}{\mu} = \sin \beta \quad (16)$$

where  $\beta$  is the angle between the ETDM and the channel axis (coinciding with  $z$ -axis),  $\mu$  is the length of the ETDM, and  $\mu_{xy}$  is its projection to  $x,y$ -plane, as shown in Scheme 10, for the extinction coefficient of dye in monolayer one gets:

$$\varepsilon_M = \frac{3}{2} \varepsilon \sin^2 \beta \quad (17)$$

where  $\varepsilon$  is the extinction coefficient in anisotropic media.

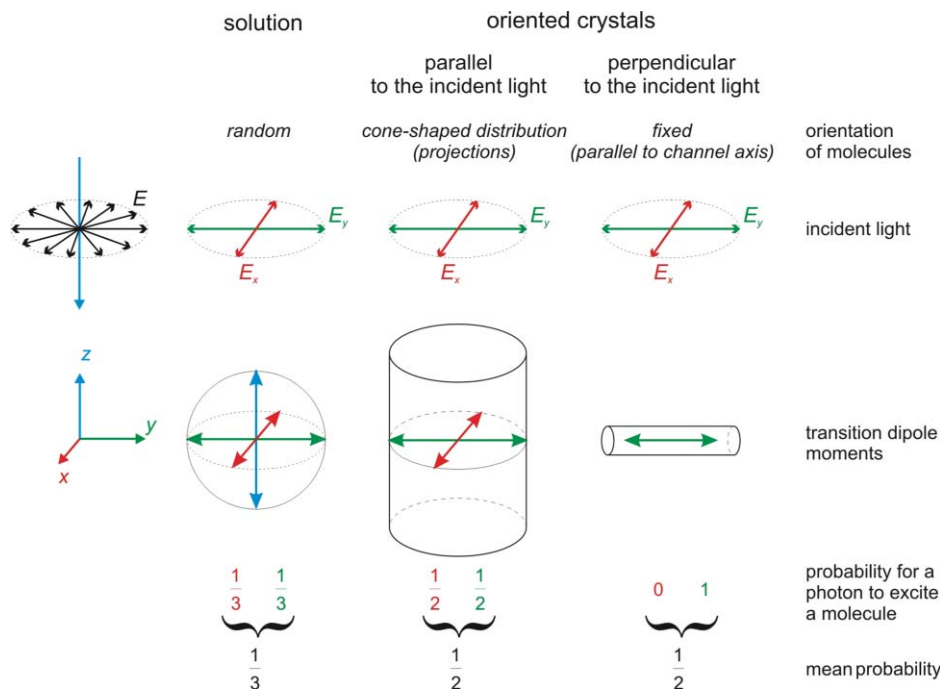
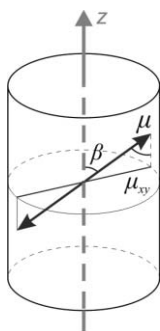


**Fig. 39** Probability for a photon to excite a molecule in solution in a dye-loaded zeolite L monolayer and in systems consisting of parallel zeolite crystals loaded with molecules oriented along the channels. The unpolarized incident light is represented by two photons,  $E_x$  and  $E_y$ , with electric vectors along the  $x$ - and  $y$ -axis, respectively.



**Scheme 10** Projection of the ETDM on the  $x,y$ -plane.

The third situation in Fig. 39 refers to molecules with fixed orientation of the ETDM in the  $x,y$ -plane. This situation occurs in systems where crystals are arranged in nematic phase or in parallel straight chains as shown in Fig. 40 and filled with molecules with ETDM oriented along the channels axis. In this case, all ETDM are aligned along one axis,  $y$ -axis in our case. Thus, photon  $E_y$  possesses a probability of one to excite a molecule, while the  $E_x$  has a probability of zero. The mean probability is the same as for a monolayer, namely  $1/2$ . Here we have an interesting situation where the extinction coefficient of the system depends on the polarization of the incident light. If light is unpolarized, the extinction coefficient is  $\frac{3}{2}\epsilon$ . If light is polarized, one of three cases takes place: (i) Light polarization coincides with the orientation of the ETDM,  $\theta = 0^\circ$ . ( $\theta$  is the angle between polarization of light,  $E$ , and the ETDM as show in Fig. 40). The extinction coefficient is then  $3\epsilon$ . (ii) Light polarized perpendicular to the ETDM,  $\theta = 90^\circ$ . The extinction coefficient is zero. (iii) Light polarized at  $0^\circ < \theta < 90^\circ$ . The extinction coefficient is equal to  $3\epsilon\cos\theta$ .

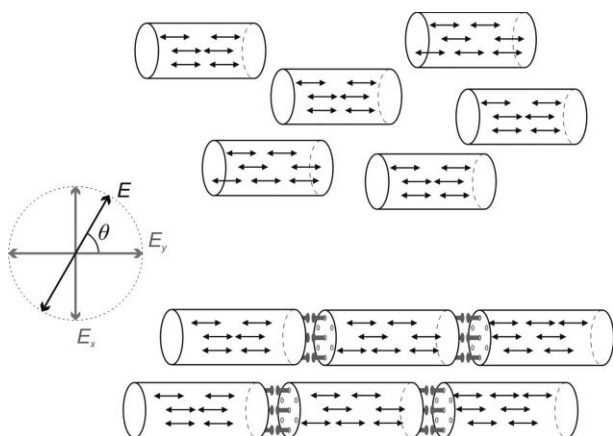


**Fig. 40** Fixed orientation of the ETDM in the  $x,y$ -axis: crystals are filled with molecules with ETDM oriented along the channels axis and arranged in nematic phase (top) or in parallel straight chains (bottom).  $\theta$  describes the angle between the polarisation of incident light,  $E$ , and the ETDM (coinciding with  $E_y$  in this example).

### 9.3. Absorption spectra to determine the dye loading in dye-zeolite L monolayers

In this Section we obtain the expression to calculate the loading of a monolayer from the absorption spectrum measured when light falls perpendicular to the monolayer support ( $\alpha = 90^\circ$ ).

The first step is to get rid of the remaining scattering. One can do this assuming the  $1/\lambda^4$  dependence of Rayleigh scattering of zeolite L.<sup>131,132</sup> The dye concentration can be found from the Beer-Lambert law:

$$A = \epsilon cd \quad (18)$$

where  $\epsilon$  is the molar extinction coefficient in  $M^{-1}cm^{-1}$ ,  $c$  is the concentration in  $mol L^{-1}$  and  $d$  is the path length of the light beam in cm; for the monolayer,  $d$  is the length of zeolite crystals. Hence, the concentration of dye in the monolayer is obtained by taking eqn (17) for  $\epsilon_M$  into account

$$c = \frac{2}{3} \frac{A}{\epsilon d \sin \beta} \quad (19)$$

Since when measuring the absorption spectrum the light beam illuminates many crystals, one should take into account empty space, or void, between the crystals. No absorption happens in these regions, hence, the dye concentration in zeolite crystals is higher than that proposed by the previous formula. The percentage of void area is easy to calculate when assuming cylindrically shaped crystals arranged as shown in Fig. 41. Then in a square of length  $2r$ , the ratio of areas void to square is 0.215, *i.e.* the dye concentration in crystals is 21.5% higher:

$$c = 0.81 \frac{A}{\epsilon d \sin \beta} \quad (20)$$

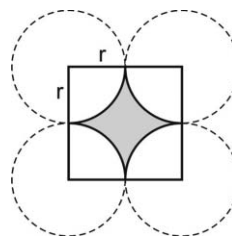


**Fig. 41** Top view of standing crystals of a monolayer. There is an empty volume, or void, between the crystals. No absorption happens there.

It is more convenient to have the expression where the length  $L$  of the crystals is expressed in nm:

$$c = 0.81 \times 10^7 \frac{A}{\epsilon L \sin \beta} \quad (21)$$

The expression for the loading  $p$  is obtained by using eqn (7):

$$p = 1.076 \times 10^7 \frac{An_s}{\epsilon L \sin \beta} \quad (22)$$

## 10. Summary

One of the most fascinating topics of modern photochemistry is the preparation and investigation of hierarchically organized structures, presenting successive ordering from the molecular up to macroscopic scale, thus supporting the relationship between the molecular arrangements and the macroscopic properties, and eventually combining them with objects that respond to a light input realized by means of near field interaction. We have shown that such structures can be built by means of host-guest chemistry where the host is a zeolite L crystal of different size and morphology and where the guests are dye molecules.

Communication between the chromophores located inside of the host and the outside world is realized *via* stopcock molecules of different shape, size and nature. The host–guest nano- to micro-objects can be organized in different patterns so that systems with distinct macroscopic properties result. The new materials and procedures can be applied in the development of novel optical and electrooptical devices, for analytical purposes and for diagnostics. They are very attractive for being investigated by means of linear and nonlinear fluorescence microscopy techniques and they provide photochemist with fascinating possibilities for solving old problem and creating new options.

## Acknowledgements

This work was financially supported by the Clariant Ltd. Research Project *Dye-Loaded Zeolites*. G. Calzaferri also thanks Prof. L. De Cola, for financial support during his stay at the University of Münster and for many important discussions. We would also like to thank Dr Roman Bolliger, Dr Viktor Shklover, Dr Stefan Huber, Dr Arantzazu Zabala Ruiz, André Mätzener and Simon Fahrni for their contributions to the Fig. 7, 3(B), 17, 29, 6 and 38, respectively and Dr André Devaux for his assistance to realize this manuscript.

## References

- Govindjee and W. Coleman, Wie Pflanzen Sauerstoff produzieren, *Spektrum der Wissenschaft*, 1990, **4**, 92–99.
- A. Currao, V. Raja Reddy, M. K. van Veen, R. E. I. Schropp and G. Calzaferri, Water splitting with silver chloride photoanodes and amorphous silicon solar cells, *Photochem. Photobiol. Sci.*, 2004, **3**, 1017–1025.
- V. R. Reddy, A. Currao and G. Calzaferri, Zeolite A and zeolite L monolayers modified with AgCl as photocatalyst for water oxidation to O<sub>2</sub>, *J. Mater. Chem.*, 2007, **17**, 3603–3609.
- P. Würfel, *Physics of Solar Cells. From Principles to New Concepts*, Wiley-VCH, Weinheim, 2005.
- X. Hu and K. Schulten, How nature harvests sunlight, *Phys. Today*, 1997, **50**, 28–34.
- T. Ritz, A. Damjanović and K. Schulten, The quantum physics of photosynthesis, *ChemPhysChem*, 2002, **3**, 243–248.
- V. May and O. Kühn, *Charge and Energy Transfer Dynamics in Molecular Systems*, Wiley VCH, Weinheim, 2nd edn, 2004.
- R. van Grondelle and V. I. Novoderezhkin, Energy transfer in photosynthesis: experimental insights and quantitative models, *Phys. Chem. Chem. Phys.*, 2006, **8**, 793–807.
- Th. Förster, Energiewanderung und Fluoreszenz, *Die Naturwissenschaften*, 1946, **6**, 166–175.
- Th. Förster, Zwischenmolekulare Energiewanderung und Fluoreszenz, *Ann. Phys.*, 1948, **437**, 55–75.
- Th. Förster, *Fluoreszenz Organischer Verbindungen*, Vandenhoeck & Ruprecht, Göttingen, 1951.
- G. D. Scholes, C. Curutchet, B. Mennucci, R. Cammi and J. Tomasi, How solvent controls electronic energy transfer and light harvesting, *J. Phys. Chem. B*, 2007, **111**, 6978–6982.
- V. Balzani, M. Venturi and A. Credi, *Molecular Devices and Machines. A Journey into the Nanoworld*, Wiley-VCH, Weinheim, 2003.
- C.-H. Chen, K.-Y. Liu, S. Sudhakar, T.-S. Lim, W. Fann, C.-P. Hsu and T.-Y. Luh, Efficient light harvesting and energy transfer in organic-inorganic hybrid multichromophoric materials, *J. Phys. Chem. B*, 2005, **109**, 17887–17891.
- N. J. Turro, From boiling stones to smart crystals: supramolecular and magnetic isotope control of radical–radical reactions in zeolites, *Acc. Chem. Res.*, 2000, **33**, 637–646.
- G. Schulz-Ekloff, D. Wöhrle, B. van Duffel and R. A. Schoonheydt, Chromophores in porous silicas and minerals: preparation and optical properties, *Microporous Mesoporous Mater.*, 2002, **51**, 91–138.
- S. Hashimoto, Zeolite photochemistry: Impact of zeolites on photochemistry and feedback from photochemistry to zeolite science, *Photochem. Photobiol. C*, 2003, **4**, 19–49.
- A. Corma and H. Garcia, Supramolecular host–guest systems in zeolites prepared by ship-in-a-bottle synthesis, *Eur. J. Inorg. Chem.*, 2004, 1143–1164.
- M. N. Chrétien, Supramolecular photochemistry in zeolites: From catalysts to sunscreens, *Pure Appl. Chem.*, 2007, **79**, 1–20.
- S. Hashimoto, M. Hagiri, N. Matsubara and S. Tobita, Photophysical studies of neutral aromatic species confined in zeolite L: Comparison with cationic dyes, *Phys. Chem. Chem. Phys.*, 2001, **3**, 5043–5051.
- S. Hashimoto, H. R. Moon and K. B. Yoon, Optical microscopy study of zeolite-dye composite materials, *Microporous Mesoporous Mater.*, 2007, **101**, 10–18.
- G. Calzaferri and N. Gfeller, Thionine in the cage of zeolite L, *J. Phys. Chem.*, 1992, **96**, 3428–3435.
- F. Binder, G. Calzaferri and N. Gfeller, Dye molecules in zeolites as artificial antenna, *Sol. Energy Mater. Sol. Cells*, 1995, **38**, 175–186.
- G. Calzaferri, Zeolite microcrystals as hosts for supramolecular organization of dye molecules, *Chimia*, 1998, **52**, 525–532.
- N. Gfeller and G. Calzaferri, Energy migration in dye-loaded hexagonal microporous crystals, *J. Phys. Chem.*, 1997, **101**, 1396–1408.
- N. Gfeller, S. Megelski and G. Calzaferri, Transfer of electronic excitation energy between dye molecules in the channels of zeolite L, *J. Phys. Chem. B*, 1998, **102**, 2433–2436.
- G. Calzaferri, S. Huber, H. Maas and C. Minkowski, Host–guest antenna materials, *Angew. Chem., Int. Ed.*, 2003, **42**, 3732–3758.
- G. Calzaferri, H. Maas, M. Pauchard, M. Pfenniger, S. Megelski and A. Devaux, Supramolecularly organized luminescent dye molecules in the channels of zeolite L, in *Advances in Photochemistry*, Vol. 27, ed. D. C. Neckers, G. von Bünau and W. S. Jenks, John Wiley & Sons, Hoboken NJ, 2002, pp. 1–50.
- D. W. Breck, *Zeolite Molecular Sieves*, John Wiley & Sons, New York, 1974.
- S. Ernst and J. Weitkamp, Synthesis of large pore aluminosilicates, *J. Catal. Today*, 1994, **19**, 27–60.
- Ch. Baerlocher, W. M. Meier and D. H. Olson, *Atlas of Zeolite Framework Types*, Elsevier, Amsterdam, 5th edn, 2001.
- T. Ohsuna, B. Slater, F. Gao, J. Yu, Y. Sakamoto, G. Zhu, O. Terasaki, D. E. W. Vaughan, S. Qiu and C. R. A. Catlow, Fine structures of zeolite-Linde-L (LTL): Surface structures, growth unit and defects, *Chem.–Eur. J.*, 2004, **10**, 5031–5040.
- O. Larlus and V. P. Valtchev, Crystal morphology control of LTL-type zeolite crystals, *Chem. Mater.*, 2004, **16**, 3381–3389.
- Y.-J. Lee, J. S. Lee and K. B. Yoon, Synthesis of long zeolite-L crystals with flat facets, *Microporous Mesoporous Mater.*, 2005, **80**, 237–246.
- T. Ban, H. Saito, Miyoshi Naito, Y. Ohya and Y. Takahashi, Synthesis of zeolite L crystals with different shapes, *J. Porous Mater.*, 2007, **14**, 119–126.
- S. Megelski and G. Calzaferri, Tuning the size and shape of zeolite L based inorganic/organic host/guest composites for optical antenna systems, *Adv. Funct. Mater.*, 2001, **11**, 277–286.
- A. Zabala Ruiz, D. Brühwiler, T. Ban and G. Calzaferri, Synthesis of zeolite L: tuning size and morphology, *Monatshefte für Chemie*, 2005, **136**, 77–89.
- A. Zabala Ruiz, D. Brühwiler, L.-Q. Dieu and G. Calzaferri, Controlling size and morphology of zeolite L, in *Materials Syntheses, A practical Guide*, ed. U. Schubert, N. Hüsing and R. Laine, Springer, Wien, 2008, (ISBN 978-3-211-75124-4).
- www.nano.zeolite.clariant.com.
- M. Pauchard, A. Devaux and G. Calzaferri, Dye-loaded zeolite L sandwiches as artificial antenna systems for light transport, *Chem.–Eur. J.*, 2000, **6**, 3456–3470.
- A. Devaux, C. Minkowski and G. Calzaferri, Electronic and vibrational properties of fluorenone in the channels of zeolite L, *Chem.–Eur. J.*, 2004, **10**, 2391–2408.
- O. Bossart and G. Calzaferri, Organisation and solubilisation of zeolite L crystals, *Chimia*, 2006, **60**, 179–181.
- C. Minkowski, R. Pansu, M. Takano and G. Calzaferri, Energy collection, transport, and trapping by supramolecular organization of dyes in hexagonal zeolite nano crystals, *Adv. Funct. Mater.*, 2006, **16**, 273–285.
- S. Huber, A. Zabala Ruiz, H. Li, G. Patrinoiu, Ch. Botta and G. Calzaferri, Optical spectroscopy of inorganic-organic host–guest

- nanocrystals organized as oriented monolayers, *Inorg. Chim. Acta*, 2007, **360**, 869–875.
- 45 R. Q. Albuquerque and G. Calzaferri, Proton activity inside the channels of zeolite L, *Chem.–Eur. J.*, 2007, **13**, 8939–8952.
  - 46 D. Brühwiler, N. Gfeller and G. Calzaferri, Resorufin in the channels of zeolite L, *J. Phys. Chem. B*, 1998, **102**, 2923–2929.
  - 47 M. Pfenniger and G. Calzaferri, Intrazeolite diffusion kinetics of dye molecules in the nano channels of zeolite L monitored by energy transfer, *ChemPhysChem*, 2000, **1**, 211–217.
  - 48 R. Hoppe, G. Schulz-Ekloff, D. Wöhrle, C. Kirschhock, H. Fuess, L. Uytterhoeven and R. Schoonheydt, Incorporation of methylene blue in NaY Zeolite at crystallographically defined positions, *Adv. Mater.*, 1995, **7**, 61–64.
  - 49 B. Hennessy, S. Megelski, C. Marcolli, V. Shklover, C. Bärlocher and G. Calzaferri, Characterization of methylviologene in the channels of zeolite L, *J. Phys. Chem. B*, 1999, **103**, 3340–3351.
  - 50 P. Simoncic and T. Armbruster, Cationic methylene blue incorporated into zeolite mordenite-Na: a single crystal X-ray study, *Microporous Mesoporous Mater.*, 2005, **81**, 87–95.
  - 51 C. Baetz and H. Fuess, Organic guest molecules in zeolites, in *Host-Guest Systems based on Nanoporous Crystals*, ed. F. Laeri, F. Schüth, U. Simon and M. Wark, Wiley-VCH, Weinheim, 2003, p. 3.
  - 52 V. Ramamurthy, J. V. Caspar and D. R. Corbin, Triplet-state photophysics of naphthalene and a,o-diphenylpolyenes included in heavy-atom-exchanged zeolites, *J. Phys. Chem.*, 1990, **94**, 3391–3393.
  - 53 V. Ramamurthy, J. V. Caspar, D. R. Corbin and D. E. Eaton, Modification of photochemical reactivity by zeolites: Arrested molecular rotation of polyenes by inclusion in zeolites, *J. Photochem. Photobiol., A*, 1990, **51**, 259–263.
  - 54 J. V. Caspar, V. Ramamurthy and D. R. Corbin, The location of organic guests within X-Type faujasite zeolites via external heavy-atom induced phosphorescence, *Coord. Chem. Rev.*, 1990, **97**, 225–263.
  - 55 V. Ramamurthy, Photoprocesses of organic molecules included in zeolites, in *Photochemistry in Organized and Constrained Media*, ed. V. Ramamurthy, VCH publishers, New York, 1991, pp. 429–493.
  - 56 S. Megelski, A. Lieb, M. Pauchard, A. Drechsler, S. Glaus, C. Debus, A. J. Meixner and G. Calzaferri, Orientation of fluorescent dyes in the nano channels of zeolite L, *J. Phys. Chem. B*, 2001, **105**, 25–35.
  - 57 E. G. McRae and M. Kasha, The molecular exciton model, in *Physical Progress in Radiation Biology*, Academic Press, New York, 1964, pp. 23–42.
  - 58 T. Kobajashi, *J-Aggregates*, World Scientific, Singapore, 1996.
  - 59 L. D. Bakalisand and J. Knoester, Pump–probe spectroscopy and the exciton delocalization length in molecular aggregates, *J. Phys. Chem. B*, 1999, **103**, 6620–6628.
  - 60 A. S. R. Koti, J. Taneja and N. Periasamy, Control of coherence length and aggregate size in the J-aggregate of porphyrin, *Chem. Phys. Lett.*, 2003, **375**, 171–176.
  - 61 A. S. Davidov, The theory of molecular excitons, *Soviet Physics - Uspekhi*, 1964, **82**, 145–178.
  - 62 M. Busby, C. Blum, M. Tibben, S. Fibikar, G. Calzaferri, V. Subramaniam and L. De Cola, Time, space and spectrally resolved studies on J-aggregate interactions in zeolite-L nanochannels, *J. Am. Chem. Soc.*, in press.
  - 63 K. Lutkouskaya, *Fluorescence properties of dye–zeolite L nanochannel materials*, University of Bern, 2007.
  - 64 P. R. Hammond, Self-absorption of molecular fluorescence, the design of equipment for measurement of fluorescence decay, and the decay times of some laser dyes, *J. Chem. Phys.*, 1979, **70**, 3884–3894.
  - 65 M. Pauchard, S. Huber, R. Méallet-Renault, H. Maas, R. Pansu and G. Calzaferri, Time- and space-resolved luminescence of a photonic dye–zeolite antenna, *Angew. Chem., Int. Ed.*, 2001, **40**, 2839–2842.
  - 66 C. Minkowski and G. Calzaferri, Förster-type energy transfer along a specified axis, *Angew. Chem., Int. Ed.*, 2005, **117**, 5459–5463.
  - 67 K. Lutkouskaya and G. Calzaferri, Transfer of electronic excitation energy between randomly mixed dye molecules in the channels of zeolite L, *J. Phys. Chem. B*, 2006, **110**, 5633–5638.
  - 68 G. Calzaferri, D. Brühwiler, S. Megelski, M. Pfenniger, M. Pauchard, B. Hennessy, H. Maas, A. Devaux and U. Graf, Playing with dye molecules at the inner and outer surface of zeolite L, *Solid State Sci.*, 2000, **2**, 421–447.
  - 69 J. P. S. Farinha, J. G. Spiro and M. A. Winnik, Energy transfer in the restricted geometry of lamellar block copolymer interfaces, *J. Phys. Chem. B*, 2001, **105**, 4879–4888.
  - 70 M. M. Yatskou, M. Meyer, S. Huber, M. Pfenniger and G. Calzaferri, Electronic excitation energy migration in a photonic dye–zeolite antenna, *ChemPhysChem*, 2003, **4**, 567–587.
  - 71 G. Calzaferri, Dye-loaded zeolite materials, *US and EU patent*, WO 02/36490 A1, priority date 2000, granted US 2005, EU 2006.
  - 72 S. Huber and G. Calzaferri, Energy transfer from dye–zeolite L antenna crystals to bulk silicon, *ChemPhysChem*, 2004, **5**, 239–242.
  - 73 A. Zabala Ruiz, *Unidirectional photonic antenna systems*, University of Bern, 2006.
  - 74 G. Calzaferri, M. Pauchard, H. Maas, S. Huber, A. Khatyr and T. Schaafsma, Photonic antenna system for light harvesting, transport and trapping, *J. Mater. Chem.*, 2002, **12**, 1–13.
  - 75 C. Marcolli and G. Calzaferri, Monosubstituted Octasilasesquioxanes, *Appl. Organomet. Chem.*, 1999, **13**, 213–226.
  - 76 A. Khatyr, H. Maas and G. Calzaferri, Synthesis of new molecules containing head, spacer and label, *J. Org. Chem.*, 2002, **67**, 6705–6710.
  - 77 L.-Q. Dieu, A. Devaux, I. López-Duarte, M. V. Martínez-Díaz, D. Brühwiler, G. Calzaferri and T. Torres, Novel phthalocyanine-based stopcock for zeolite L, *Chem. Commun.*, 2008, 1187–1198.
  - 78 W. Spahn and G. Calzaferri, Synthese von *para*-substituierten Phenyl-Terpyridin Liganden, *Helv. Chim. Acta*, 1984, **67**, 450–454.
  - 79 Z. Popović, M. Busby, S. Huber, G. Calzaferri and L. De Cola, Assembling micro crystals via cooperative nano scale interactions, *Angew. Chem., Int. Ed.*, 2007, **46**, 8898–8902.
  - 80 G. Calzaferri, S. Huber, A. Devaux, A. Zabala Ruiz, H. Li, O. Bossart and L.-Q. Dieu, Light-harvesting host–guest antenna materials for photonic devices, in *Proc. SPIE-Org. Optoelectr. Photonics II*, 2006, **6192**, 619216-1-9.
  - 81 R. Ziessel, C. Goze, G. Ulrich, M. Césario, P. Retailleau, A. Harriman and J. P. Rostron, Intramolecular energy transfer in pyrene-bodipy molecular dyads and triads, *Chem.–Eur. J.*, 2005, **11**, 7366–7378.
  - 82 H. Maas and G. Calzaferri, Constructing dye–zeolite photonic nanodevices, *Spectrum*, 2003, **16**, 18–24.
  - 83 O. Bossart, L. De Cola, S. Welter and G. Calzaferri, Injecting electronic excitation energy into an artificial antenna system by a Ru<sup>2+</sup> complex, *Chem.–Eur. J.*, 2004, **10**, 5771–5775.
  - 84 H. Maas and G. Calzaferri, Trapping energy from and injecting energy into dye–zeolite nanoantennae, *Angew. Chem., Int. Ed.*, 2002, **41**, 2284–2287.
  - 85 T. Ban, D. Brühwiler and G. Calzaferri, Selective modification of the channel entrances of zeolite L with triethoxysilylated coumarin, *J. Phys. Chem. B*, 2004, **108**, 16348–16352.
  - 86 H. Li, A. Devaux, Z. Popović, L. De Cola and G. Calzaferri, Carboxyester functionalised dye–zeolite L host–guest materials, *Microporous Mesoporous Mater.*, 2006, **95**, 112–117.
  - 87 H. Maas, *Energy transfer at the frontiers of dye-loaded zeolite L*, University of Bern, 2003.
  - 88 S. Huber and G. Calzaferri, Sequential functionalization of the channel entrances of zeolite L crystals, *Angew. Chem., Int. Ed.*, 2004, **43**, 6738–6742.
  - 89 R. Koeppe, O. Bossart, G. Calzaferri and N. S. Sariciftci, Advanced photon harvesting concepts for low energy gap organic solar cells, *Sol. Energy Mater. Sol. Cells*, 2007, **91**, 986–995.
  - 90 G. Calzaferri, O. Bossart, D. Brühwiler, S. Huber, C. Leiggenger, M. K. van Veen and A. Zabala, Ruiz, Light-harvesting host–guest antenna materials for quantum solar energy conversion devices, *C. R. Chimie*, 2006, **9**, 214–225.
  - 91 M. A. Coutant, P. Payra and P. K. Dutta, Oxygen transport in zeolite Y measured by quenching of encapsulated tris(bipyridyl)ruthenium, *Microporous Mesoporous Mater.*, 2003, **60**, 79–90.
  - 92 P. Payra and P. K. Dutta, Development of a dissolved oxygen sensor using tris(bipyridyl) ruthenium (II) complexes entrapped in highly siliceous zeolites, *Microporous Mesoporous Mater.*, 2003, **64**, 109–118.
  - 93 J. N. Demas, E. W. Harris and R. P. McBride, Energy transfer from luminescent transition metal complexes to oxygen, *J. Am. Chem. Soc.*, 1977, **99**, 3547–3551.
  - 94 R. Q. Albuquerque, Z. Popović, L. De Cola and G. Calzaferri, Luminescence quenching by O<sub>2</sub> of a Ru<sup>2+</sup> complex with a tail attached to zeolite L, *ChemPhysChem*, 2006, **7**, 1050–1053.
  - 95 R. Q. Albuquerque, A. Zabala Ruiz, H. Li, L. De Cola and G. Calzaferri, Luminescence quenching measurements on zeolite L monolayers, in *Proceedings of SPIE, Photonics for Solar Energy Systems*, 2006, **6197**, 61970B-1-5.
  - 96 O. Bossart, *Zeolite L antenna material for organic light emitting diodes and organic solar cells*, University of Bern, 2006.

- 97 J. Kido, K. Hongawa, K. Okuyama and K. Nagai, Bright blue electroluminescence from poly(N-vinylcarbazole), *Appl. Phys. Lett.*, 1993, **63**, 2627–2629.
- 98 D. Brühwiler and G. Calzaferri, Selective functionalization of the external surface of zeolite L, *C. R. Chimie*, 2005, **8**, 391–398.
- 99 A. Laurent, F. Debart, N. Lamb and B. Rayner, Esterase-triggered fluorescence of fluorogenic oligonucleotides, *Bioconjugate Chem.*, 1997, **8**, 856–861.
- 100 T. Phuong, T. Khac-Minh, N. T. Van Ha and H. T. Ngoc, Phuong, Synthesis and antifungal activities of phenylenedithiouras, *Bioorg. Med. Chem. Lett.*, 2004, **14**, 653–656.
- 101 M. Busby, H. Kerschbaumer, G. Calzaferri and L. De Cola, Orthogonally bi-functional fluorescent zeolite-L micro-crystals, *Adv. Mater.*, 2008, **20**, 1614–1618.
- 102 P. Yang, T. Deng, D. Zhao, P. Feng, D. Pine, B. F. Chmelka, G. M. Whitesides and G. D. Stucky, Hierarchically ordered oxides, *Science (Reports)*, 1998, **282**, 2244–2246.
- 103 D. R. Walt, Top-to-bottom functional design, *Nat. Mater.*, 2002, **1**, 17–18.
- 104 A. Böker, Y. Lin, K. Chiapperini, R. Horowitz, M. Thompson, V. Carreon, T. Xu, C. Abetz, H. Skaff, A. D. Dinsmore, T. Emrick and T. P. Russell, Hierarchical nanoparticle assemblies formed by decorating breath figures, *Nat. Mater.*, 2004, **3**, 302–306.
- 105 M. Bashouti, W. Salalha, M. Brumer, E. Zussman and E. Lifshitz, Alignment of colloidal CdS nanowires embedded in polymer nanofibers by electrospinning, *ChemPhysChem*, 2006, **7**, 102–106.
- 106 S.-J. Huo, X.-K. Xue, Q.-X. Li, S.-F. Xu and W.-B. Cai, Seeded-growth approach to fabrication of silver nanoparticle films on silicon for electrochemical ATR surface-enhanced IR absorption spectroscopy, *J. Phys. Chem. B*, 2006, **110**, 25721–25728.
- 107 L. Dai, A. Patil, X. Gong, Z. Guo, L. Liu, Y. Liu and D. Zhu, Aligned nanotubes, *ChemPhysChem*, 2003, **4**, 1150–1169.
- 108 G. A. Ozin, and A. C. Arsenault, *Nanochemistry: A Chemical Approach to Nanomaterials*, RSC Publishing, Cambridge, UK, 2005.
- 109 S. J. Hurst, E. K. Payne, L. D. Qin and C. A. Mirkin, Multisegmented one-dimensional nanorods prepared by hard-template synthetic methods, *Angew. Chem., Int. Ed.*, 2006, **45**, 2672–2692.
- 110 T. Bein, Zeolitic host–guest interactions and building blocks for the selfassembly of complex materials, *MRS Bull.*, 2005, **30**, 713.
- 111 T. Bein, Host–guest interactions in zeolites and periodic mesoporous materials, in *Studies in Surface Science and Catalysis, Vol. 168: Introduction to Zeolite Science and Practice*, ed J. Cejka, H. van Bekkum, A. Corma and F. Schüth, Elsevier, Amsterdam, 3rd revised edn, 2007, pp. 611–658.
- 112 A. Gouzinis and M. Tsapatsis, On the preferred orientation and microstructural manipulation of molecular sieve films prepared by secondary growth, *Chem. Mater.*, 1998, **10**, 2497–2504.
- 113 K. B. Yoon, Organization of zeolite microcrystals for production of functional materials, *Acc. Chem. Res.*, 2007, **40**, 29–40.
- 114 J. S. Lee, H. Lim, K. Ha, H. Cheong and K. B. Yoon, Facile monolayer assembly of fluorophore-containing zeolite rods in uniform orientations for anisotropic photoluminescence, *Angew. Chem., Int. Ed.*, 2006, **45**, 5288–5292.
- 115 J. Caro, G. Finger, J. Kornatowski, J. Richter-Mendau, L. Werner and B. Zibrowius, Aligned molecular sieve crystals, *Adv. Mater.*, 1992, **4**, 273–276.
- 116 L. Scandella, G. Binder, J. Gobrecht and J. C. Jansen, Alignment of single-crystal zeolites by means of microstructured surfaces, *Adv. Mater.*, 1996, **8**, 137–139.
- 117 J. Michl and E. W. Thulstrup, Ultraviolet and infrared linear dichroism: polarized light as a probe of molecular and electronic structure, *Acc. Chem. Res.*, 1987, **20**, 192–199.
- 118 O. Bossart and G. Calzaferri, Selfassembly of zeolite L crystals on biological self-cleaning surfaces, *Microporous Mesoporous Mater.*, 2008, **109**, 392–397.
- 119 N. Bowden, A. Terfort, J. Carbeck and G. M. Whitesides, Self-assembly of mesoscale objects into ordered two-dimensional arrays, *Science (Reports)*, 1997, **276**, 233–235.
- 120 S. Yunus, F. Spano, G. Patrinoiu, A. Bolognesi, C. Botta, D. Brühwiler, A. Zabala Ruiz and G. Calzaferri, Hexagonal network organization of dye-loaded zeolite L crystals by surface tension driven auto-assembly, *Adv. Funct. Mater.*, 2006, **16**, 2213–2217.
- 121 A. Zabala Ruiz, H. Li and G. Calzaferri, Organizing supramolecular functional dye–zeolite crystals, *Angew. Chem., Int. Ed.*, 2006, **45**, 5282–5287.
- 122 G. Calzaferri, A. Zabala Ruiz, H. Li and S. Huber, Oriented zeolite material and method for producing the same, WO 2007/012216 A2, priority US 60/698,480 and CH 1266/05.
- 123 I. Cucci, F. Spano, U. Giovanella, M. Catellani, A. Varesano, G. Calzaferri and C. Botta, Fluorescent electrospun nanofibres embedding dye-loaded zeolite crystals, *Small*, 2007, **3**, 305–309.
- 124 Z. Popović, M. Otter, G. Calzaferri and L. De Cola, Self-assembling living systems with functional nanomaterials, *Angew. Chem., Int. Ed.*, 2007, **46**, 6188–6191.
- 125 H. Li, Y. Wang, W. Zhang, B. Liu and G. Calzaferri, Fabrication of oriented zeolite L monolayers employing luminescent peryleneimide-bridged Si(OEt)<sub>3</sub> precursor as the covalent linker, *Chem. Commun.*, 2007, 2853–2854.
- 126 A. Devaux, K. Lutkouskaya, G. Calzaferri, L.-Q. Dieu, D. Brühwiler, L. De Cola and T. Torres, Nanochannels for supramolecular organization of dyes, *Photochemistry in Switzerland, Special Issue CHIMIA*, 2007, **61**, 626–630.
- 127 Z. M. Huang, Y.-Z. Zhang, M. Kotaki and S. Ramakrishna, A review on polymer nanofibers by electrospinning and their applications in nanocomposites, *Compos. Sci. Technol.*, 2003, **63**, 2223–2253.
- 128 J. H. Yu, S. V. Fridrikh and G. C. Rutledge, Production of submicrometer diameter fibers by two-fluid electrospinning, *Adv. Mater.*, 2004, **16**, 1562–1566.
- 129 M. Y. Han, X. H. Gao, J. Z. Su and S. Nie, Quantum-dot-tagged microbeads for multiplexed optical coding of biomolecules, *Nat. Biotechnol.*, 2001, **19**, 631–635.
- 130 D. Brühwiler, L.-Q. Dieu and G. Calzaferri, Nanochannel materials for quantum solar energy conversion devices, *Transformation and Storage of Solar Energy, Special Issue CHIMIA*, 2007, **61**, 820–822.
- 131 A. Devaux, Z. Popović, O. Bossart, L. De Cola, A. Kunzmann and G. Calzaferri, Solubilisation of dye-loaded zeolite L nanocrystals, *Microporous Mesoporous Mater.*, 2006, **90**, 69–72.
- 132 S. Suárez, A. Devaux, J. Bañuelos, O. Bossart, A. Kunzmann and G. Calzaferri, Transparent zeolite-polymer materials with adaptable properties, *Adv. Funct. Mater.*, 2007, **17**, 2298–2306.